MODELLING OF MICROSTRUCTURE IN NOVEL HIGH STRENGTH STEEL WELDS

by
Gethin Rees
Emmanuel College

Department of Materials Science and Metallurgy
Pembroke Street
Cambridge
CB2 3QZ

A dissertation submitted for the degree of
Doctor of Philosophy
at the University of Cambridge

September 1992

Er cof am Mamgu a Dadcu

PREFACE

This dissertation describes work carried out between October 1988 and September 1992 at the Department of Materials Science and Metallurgy, Cambridge University, under the supervision of Dr. H.K.D.H. Bhadeshia. Unless appropriately referenced the work is my own and not the result of any collaboration. No part of this dissertation has been previously submitted for any degree or diploma at this, or any other University. The work described in Chapters 3 and 4 has been accepted for publication in the October 1992 edition of Materials Science & Technology.

This dissertation contains less than 60,000 words.

Gethin Rees

ACKNOWLEDGEMENTS

I would like to express my gratitude to my supervisor H.K.D.H. Bhadeshia for his constant enthusiasm throughout the past few years, especially during 'difficult' periods. I am greatly indebted to all members of the technical staff at the department of Materials Science & Metallurgy, Mr. Ted Pettit in particular.

During the past three and a half years I have had the pleasure of working with many amusing and interesting people from all around the world. I send my best wishes to all past members of the group, but must mention Peter Wilson, Moazam Baloch, Naseem Haddad and Suresh Babu in particular. I would also like to thank all my friends currently working hard at their research in the group. My team-mates from C.U.K.C. have also helped make my time in Cambridge very enjoyable.

Finally, thanks are due to Professor Colin Humphreys for the provision of laboratory facilities, and to Lars-Eric Svensson and ESAB (Sweden) for funding the project.

CONTENTS

CHAPTER 6 Modelling the Microstructure and Properties of High Strength Steel Welds

NOMENCLATURE

α	Ferrite (body centered cubic iron or steel).
α_1	Parabolic thickening rate constant for allotriomorphic ferrite growth.
β	Autocatalysis constant occurring in Bhadeshia's bainite transformation kinetics model.
δ	High-temperature ferrite (body centered cubic iron or steel)
ϵ_1, ϵ_2	Material dependent constant used in modelling the cooling behaviour of welds.
γ	Austenite (face centered cubic iron).
η	Arc transfer efficiency.
θ	The maximum extent of bainite transformation that can form at a given temperature.
λ_1, λ_2	Empirical constants arising in the modified bainite transformation kinetics model.
$\mu_C^{\alpha 0}$	Chemical potential of carbon in ferrite, referred to its standard state.
$\mu_{Fe}^{\alpha 0}$	Chemical potential of iron in ferrite, referred to its standard state.
$\mu_C^{\gamma 0}$	Chemical potential of carbon in austenite, referred to its standard state.
$\mu_{Fe}^{\gamma 0}$	Chemical potential of iron in ferrite, referred to its standard state.
ν	Attempt frequency for nucleation.
ξ	Normalised volume fraction of bainite *i.e.* v/θ.
ρ	Molar area density of atoms in the planes of a martensitic embryo.
σ	Total surface energy of a martensitic embryo.
σ_y	Overall yield strength of a weld microstructure.
σ_{α_a}	The contribution of acicular ferrite to the yield strength of a weld microstructure.
$\sigma_{\alpha'}$	The contribution of martensite to the yield strength of a weld microstructure.
σ_{mic}	The microstructural contribution to the strength of acicular ferrite.
τ_μ	Athermal component of the flow stress for interface dislocation motion during martensitic nucleation.
τ_i	Incubation time for reaction initiation at a given temperature.
a	Side length of hexagonal columnar austenite grains in a weld.
a_C^α	Activity of carbon in the ferrite phase.
a_C^γ	Activity of carbon in the austenite phase.
a_{Fe}^α	Activity of iron in the ferrite phase.
a_{Fe}^γ	Activity of iron in the ferrite phase.
Ae_1	The ferrite/(ferrite & austenite) equilibrium phase boundary.
Ae_3	The austenite/(ferrite & austenite) equilibrium phase boundary.
A	Area of planes in a martensitic embryo.
b	Magnitude of the Burgers vector in body centered cubic steel.

$c_1^{\gamma\alpha}$	Concentration of carbon in austenite at a ferrite/austenite phase boundary in a ternary alloy.
$c_1^{\alpha\gamma}$	Concentration of carbon in ferrite at a ferrite/austenite phase boundary in a ternary alloy.
$c_2^{\gamma\alpha}$	Concentration of the substitutional solute in austenite at a ferrite/austenite phase boundary in a ternary alloy.
$c_2^{\gamma\alpha}$	Concentration of the substitutional solute in ferrite at a ferrite/austenite phase boundary in a ternary alloy.
C_2, C_3, C_4	Empirical constants arising in Bhadeshia's bainite transformation kinetics model.
D_{11}	Diffusion coefficient of carbon in austenite.
D_{22}	Diffusion coefficient of the substitutional solute in austenite in a ternary alloy.
$\underline{D}_{11}$	Weighted average diffusion coefficient of carbon in austenite.
E^{str}	Molar strain energy of martensite nucleation.
G^*	Activation energy for nucleation of Widmanstätten ferrite or bainite.
G^α	Free energy of the ferrite phase.
G^γ	Free energy of the ferrite phase.
$G^{\gamma\rightarrow\alpha'}$	Free energy change for transformation of austenite to ferrite of identical composition.
G_N	The critical value of ΔG_m required for nucleation of displacive transformation products.
ΔG_m	Maximum free energy change per mole of precipitate phase.
ΔG_m^0	Maximum free energy change per mole of ferrite at the onset of the bainite transformation.
ΔG_m^v	Maximum volume free energy change on nucleation.
ΔG^{chem}	Molar chemical free energy change for the austenite to ferrite transformation during martensite nucleation.
G_{SW}	The minimum driving force at which growth of Widmanstätten ferrite is possible.
$\Delta\overline{H}_\alpha$	Partial molar enthalpy for solid solution of carbon in ferrite.
$\Delta\overline{H}_\gamma$	Partial molar enthalpy for solid solution of carbon in austenite.
I_{WS}	Nucleation rate of bainite at the W_S temperature (Bhadeshia 1982).
I_0	Nucleation rate of bainite at the W_S temperature, independent of the effects of autocatalysis (Bhadeshia 1982).
k	Solute partitioning coefficient.
K_1', K_2	Empirical constants arising in the modified bainite transformation kinetics model.
$\overline{L}$	Mean linear intercept of a series of random lines with the austenite grain boundaries in a sample.
n	Number of planes in a given martensitic embryo.
N	Nucleation rate of ferrite at the highest temperature of the lower. C–curve in a TTT diagram
q	Thickness of allotriomorphic ferrite layers decorating prior austenite grains.

Q	Activation energy for martensitic nucleation, alternatively the electrical heat input to an arc weld.
Q_d	Molar enthalpy of diffusion.
R	Universal gas constant.
$\Delta\overline{S}_\alpha$	Partial molar non–configurational entropy for solid solution of carbon in ferrite.
$\Delta\overline{S}_\gamma$	Partial molar non–configurational entropy enthalpy for solid solution of carbon in austenite.
S_d	Molar entropy of diffusion.
S_v	Grain boundary surface area per unit volume.
T	Temperature.
T_0	Initial temperature during the cooling of an arc weld, alternatively, the temperature at which austenite and ferrite of the same composition have identical free energies.
T_{int}	Interpass temperature for multi-run welds.
t_c	Limiting time for growth of Widmanstätten ferrite before impingement with intragranularly nucleated transformation products occurs.
T_H	Highest temperature in the lower C–curve of TTT diagrams.
T_h	The temperature at which allotriomorphic ferrite formation begins during the cooling of a weld.
t_i	The length of the ith isothermal hold time when approximating a continuous cooling curve as a series of isothermal steps.
t_m	Experimentally measured time taken to form a given volume fraction of bainite.
t_p	Predicted time taken to form a given volume fraction of bainite.
u	Volume of a bainitic sub-unit.
v	Volume fraction of ferrite in a ferrite/austenite mixture.
v^*	Activation volume of a martensitic nucleus.
V_{α_a}	Volume fraction of acicular ferrite in a microstructure.
V_α	Volume fraction of allotriomorphic ferrite in a microstructure.
$V_{\alpha w}$	Volume fraction of Widmanstätten ferrite in a microstructure.
$V_{\alpha'}$	Volume fraction of martensite in a microstructure.
V_{int}	Velocity of the α/γ interface during allotriomorphic ferrite growth.
w_α	Carbon-carbon interaction energy in ferrite.
w_γ	Carbon-carbon interaction energy in austenite.
W	Total energy of a martensitic embryo.
$\overline{x}$	Carbon mole fraction of the bulk alloy.
X	General representation of the substitutional solute in a ternary alloy steel.
x^α	Carbon mole fraction of ferrite.

x^{γ}	Carbon mole fraction of austenite.
$x^{\alpha\gamma}$	Carbon mole fraction of ferrite at the austenite/ferrite interface.
$x^{\gamma\alpha}$	Carbon mole fraction of austenite at the austenite/ferrite interface.
x_l	Liquidus composition (mole fraction).
x_m	The most probable ferrite nucleus carbon mole fraction.
x_{N_0}	Maximum austenite composition for which nucleation of ferrite by a displacive mechanism is possible.
x_s	Solidus composition (mole fraction).
$x_{T_0'}$	Composition at which austenite and ferrite (with a stored energy of 400 J mol^{-1}) have identical free energy.
Z	Position of the α/γ interface during allotriomorphic ferrite growth.

CHAPTER 1

Introduction

The aim of this chapter is to provide a brief background to the physical metallurgy of steel and to the process of welding. Both of these subjects form the cornerstone of the research topic. The theoretical concepts relevant to phase transformations work presented in later chapters are also included here.

1.1 An Introduction to the Welding Process

1.1.1 Welding Processes

The principle of fusion welding is as follows. Two pieces of metal are joined by introducing molten filler metal into the gap between them at a sufficiently high temperature to achieve some melting of the pieces being joined. Subsequent solidification of the weld metal ensures a continuous joint in which the grains of the weld metal tend to grow directly from those of the base plate.

The introduction of the filler metal can be achieved in one of many ways. One of the most common of these is arc welding, in which the heat source is an electric arc. The filler metal is introduced by the transfer of molten metal from the tip of the electrode into the joining area, where it forms a pool beneath the arc. In this process the electrode is gradually consumed, the bulk of the metal in the weld pool coming from the electrode, with some also coming from the base plate from regions beneath the arc, where its melting temperature has been exceeded. The transfer of the metal from the electrode to the weld pool occurs by a combination of many processes. These involve the gravitational pull on molten metal at the electrode tip, the electromagnetic Lorentz force resulting from the force between two current carriers, and detachment of molten metal from the electrode when contact is made between the tip and the weld pool (Lancaster, 1970). The welding current usually lies in the range 100-1000 A and the voltage in the range 10-50 V.

There are many different variants of the arc welding processes. Depending on the process the molten metal in the weld pool is protected from the surrounding environment either by shielding gasses (gas metal arc, GMA welding), or alternatively, the protection may be via a flux which forms a slag on top of the weld pool. The gasses in the air, as well as moisture, have a potentially damaging effect on the properties of the weld and so it is essential to control the extent of gas pick-up from the atmosphere. The slag therefore serves as a protective covering and can indeed provide a chemically reducing environment. Gases given off by the slag can also aid metal transfer from the electrode the weld pool.

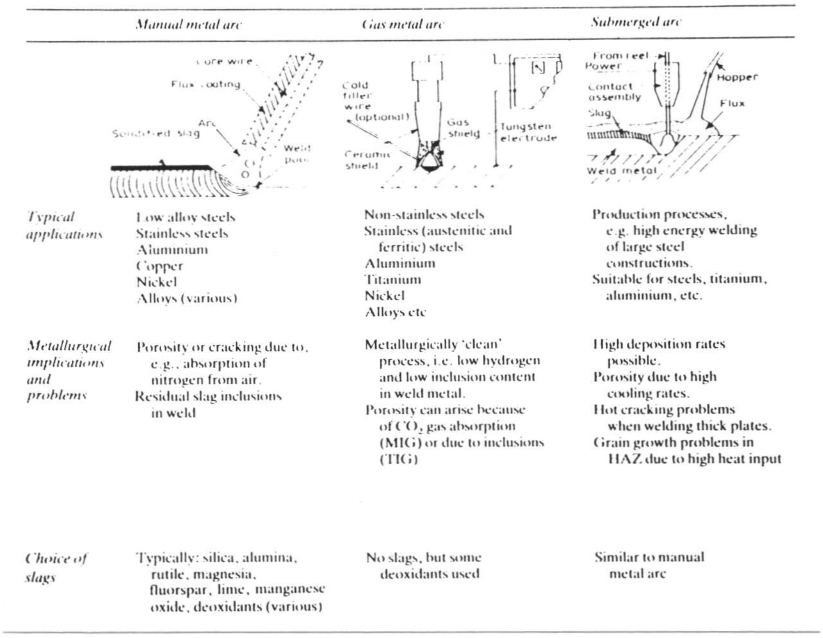

	Manual metal arc	*Gas metal arc*	*Submerged arc*
Typical applications	Low alloy steels Stainless steels Aluminium Copper Nickel Alloys (various)	Non-stainless steels Stainless (austenitic and ferritic) steels Aluminium Titanium Nickel Alloys etc	Production processes, e.g. high energy welding of large steel constructions. Suitable for steels, titanium, aluminium, etc.
Metallurgical implications and problems	Porosity or cracking due to, e.g., absorption of nitrogen from air. Residual slag inclusions in weld	Metallurgically 'clean' process, i.e. low hydrogen and low inclusion content in weld metal. Porosity can arise because of CO_2 gas absorption (MIG) or due to inclusions (TIG)	High deposition rates possible. Porosity due to high cooling rates. Hot cracking problems when welding thick plates. Grain growth problems in HAZ due to high heat input
Choice of slags	Typically: silica, alumina, rutile, magnesia, fluorspar, lime, manganese oxide, deoxidants (various)	No slags, but some deoxidants used	Similar to manual metal arc

Figure 1.1 Schematic representation of welding processes, (after Easterling 1983).

The flux derives from the electrode coating in manual metal arc welding (MMA), from an electrode core, in the case of flux cored wire welding (FCAW), or is fed directly onto the welding surface covering the arc and the electrode as in submerged arc welding (SAW), in which case the electrode can be bare. These processes are shown schematically in Figure 1.1.

This work is primarily concerned with weld deposits produced by the submerged arc technique in which flux is gravity-fed from a hopper into the path of the moving electrode. The process is very suitable for highly automated, high speed welding with large deposition rates being possible (Deb, Challenger & Therrein, 1987).

For the submerged arc process the slags typically contain silica, alumina, rutile, magnesia, flurospar, lime, manganese oxide and various deoxidants. Some oxygen is bound to ingress into the molten metal during the welding process (Grong & Matlock, 1986). The role of deoxidants is to form oxides that will separate into the slag. As the metal cools some of these deoxidation products will become trapped in the solidifying metal as inclusions. These can have an important effect on the subsequent development of the weld microstructure, as will be discussed later.

The chemical composition of the filler metal has a profound effect on the resultant microstructure of the weld metal, and therefore on the mechanical properties as well. The electrode composition determines the composition of the metal deposited into the weld pool, and together with dilution from the base plate, this controls the weldment substitutional alloy content. The carbon content of the weldment is also determined by the electrode. In general however, the electrode has a higher carbon content than the eventual deposit since oxidation of carbon occurs during the welding.

Nitrogen enters the weld pool mainly from the air. The different solubility of nitrogen in δ ferrite and austenite can cause the precipitation of nitrides as the weld metal transforms from δ to γ during cooling. Hydrogen can be inadvertently introduced through the breakdown of moisture under the influence of the electric arc, an effect that is strongly dependent on the moisture content of the flux. The extremely high diffusivity of hydrogen means that a lot of it escapes from the weld surface, however significant quantities can diffuse into the adjacent plate, causing heat affected zone cracking. Because of hydrogen's highly damaging effect on weld metal properties it is essential to eliminate its presence as much as possible. For particularly thick sections hydrogen poses even more of a problem since the surface loss of the gas is less effective in such cases.

1.1.2 The Welding Thermal Cycle

The influence of the arc extends beyond the boundary of the weld pool into the so-called heat-affected zone of the base plate. Different chemical and physical changes are expected in the weld deposit and base plate depending on the thermal experience and other characteristics of each region. As the weld is moved along the abutting plate a steady state is established between the melting and solidification processes. The shape and size of the weld pool will depend, for example, on the thermal diffusivities of the plate and molten metal, as well as the speed of welding and the heat input from the arc.

Efforts at modelling the thermal profiles resulting from welding processes have been successful in accounting for much of the behaviour exhibited by real welds. The well known work of Rosenthal (1958) considers welding as the action of a moving point heat source on a flat isotropic and homogeneous plate. In so doing the effects of changes in thermal behaviour with temperature and changes of state are ignored, as is the latent heat absorbed and released on melting and cooling. In spite of this the results are very revealing in describing the effects of the weld pass.

One interesting result is that in most cases the speed of welding exceeds that of thermal diffusivity, causing a build up of the isotherms ahead of the heat source, resulting in very steep thermal gradients in the region of the pool causing base plate melting. The heat profile of a typical submerged arc weld on a steel plate is shown in Figure 1.2.

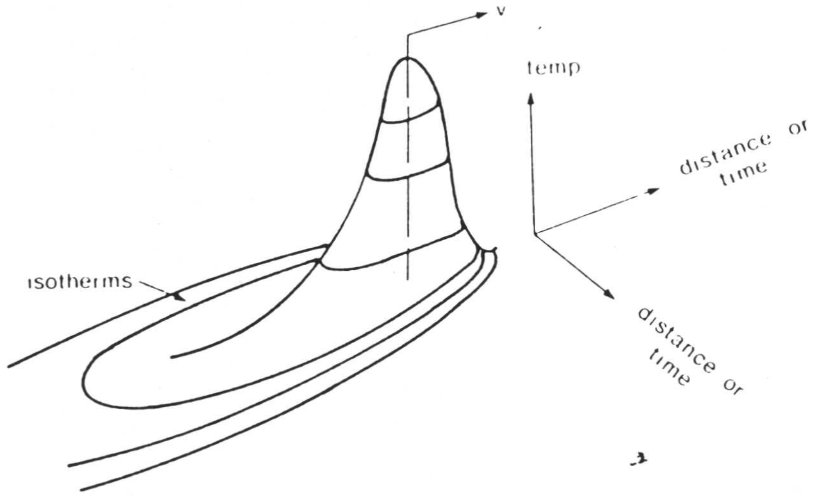

Figure 1.2 Heat profile for a submerged arc weld on a steel plate (after Easterling, 1983).

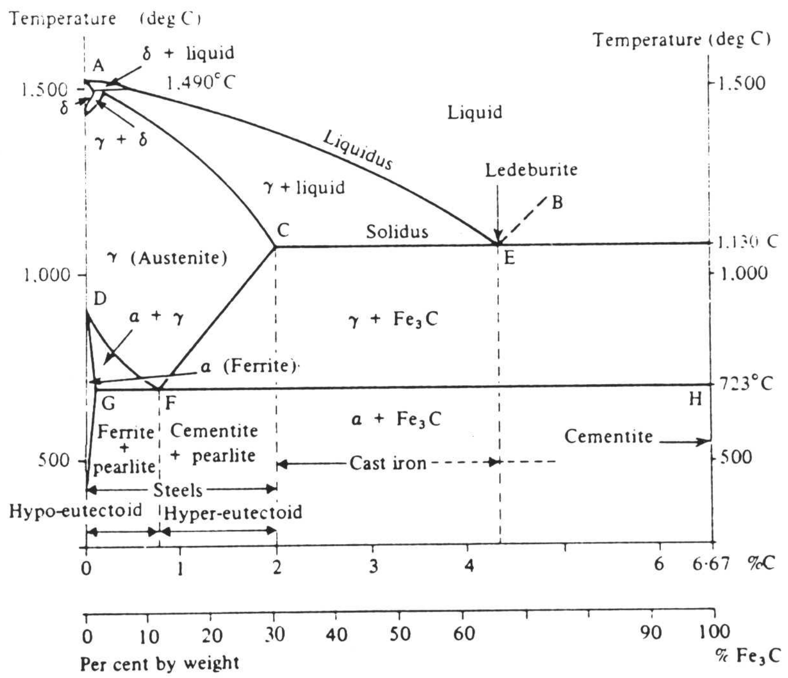

Figure 1.3 The iron–carbon phase diagram, (after Anderson *et al.*, 1985)

1.2 An Introduction to the Metallurgy of Steel

1.2.1 Pure Iron and its Allotropes

At atmospheric pressure pure iron has two allotropic forms. At low temperatures (*i.e.* $< 912°C$) the atoms form a body centered cubic structure known as ferrite (α), which is also the stable form at higher temperatures (*i.e.* $> 1394°C$). At intermediate temperatures the face centered cubic structure is the most stable, and this is called austenite, designated γ. Iron can also exist as a hexagonal close packed structure, but this is only possible at very high pressures (130 kbar). This form is known as ϵ and is the densest form of iron. Melting occurs at 1538 °C.

Iron also shows another transition. At 770 °C there is the Curie transition, which involves a change from the high temperature paramagnetic ferrite to the lower temperature ferromagnetic ferrite.

1.2.2 The Effect of Carbon and the Iron–Carbon Phase Diagram

Carbon is an interstital alloying element. Rather than replacing iron in the lattice it sits in the spaces between the iron atoms and is much more soluble in austenite than in ferrite. Varying the carbon content of steel has a significant effect on the phase transition temperatures as can be seen from the phase diagram shown in Figure 1.3.

At higher temperatures δ ferrite shows much greater carbon solubility than the very low value that α ferrite displays. At 1495 °C the δ/liquid phase field gives way to a γ/liquid field. Steels cooling through this region are said to undergo a peritectic reaction. At the transition temperature (1495 °C) three phases δ, γ and liquid can coexist as the δ and liquid react to generate austenite.

Increasing quantities of carbon confer stability to the austenite so that this field dominates the intermediate temperature range of the low carbon Fe–C diagram. A two phase α/γ region is formed as well as a similar field for the equilibrium between austenite and cementite, which is an iron carbide.

At low temperatures it can be seen that the equilibrium condition for steels with carbon contents greater than 0.0218 (wt%) is as a two phase mixture of ferrite and cementite. At just below 727 °C a steel of composition Fe–0.77 C (wt%) will be simultaneously supersaturated with respect to the ferrite and cementite phases. This results in the equilibrium structure known as pearlite where fine lamellae of α and Fe_3C form co-operatively from austenite. The lamellae are in fact interconnected in three dimensions so that each pearlite colony is actually a bicrystal of ferrite and cementite.

1.2.3 Substitutional Alloying Elements and their Effect

Another kind of alloying element is one which, in small quantities, can enter into the iron lattice replacing the host atom in the process. These elements are known as substitutional solutes. Those most commonly used in steel are silicon, manganese, nickel, molybdenum, chromium and vanadium. The presence of these elements affects the free energy change associated with the various phase transformations, therefore alloying can be used to change the transformation behaviour of steel. Substitutional alloying elements affect the Fe–C phase diagram by expanding or contracting the stability fields of the various phases, as well as changing the transition temperature between these phases. A conceptually convenient, though not rigorous notion is that those elements which expand the austenite phase field (*e.g.* C, Mn, Ni) are called austenite stabilisers, and those promoting ferrite stability are called ferrite stabilisers (*e.g.* Mo, Cr). Substitutional alloying elements can also cause the introduction of new phases such as alloy carbides.

As well as their thermodynamic effect, alloying elements usually have different solubilities in the various phases. This can necessitate redistribution during transformation. Diffusion is therefore necessary for equilibrium to be maintained. Under the correct conditions alloyed steels can be encouraged to transform at rates that do not allow for this complicated redistribution of alloying elements to take place, thereby adding further to the range of transformation structures that can be produced.

1.3 Phase Transformations in Steel

1.3.1 Equilibrium Transformations

The phases shown in the iron-carbon are the equilibrium phases, although graphite is in fact more stable that cementite. Equilibrium represents the absolute minimum free energy configuration at a given temperature and is in fact an ill-defined concept in the sense that one may have to wait for unacceptably long times for equilibrium to be achieved. A local minimum in free energy, however, gives a metastable equilibrium which follows the same thermodynamic theory. So for example, within the time scale of welding we need not worry about graphitisation and the metastable cementite phase is more appropriate for consideration.

As far as is known the phase diagram gives the minimum free energy phase or phase mixture for any given temperature. Transformation from one phase to the other must occur ideally with very slow cooling for the equilibrium structure to be attained. In practice, with sufficiently slow cooling the phases equilibrium can be maintained locally at the transformation interface, even if concentration profiles exist ahead of the advancing interface. The nucleation process in all real solid state transformations in steel is heterogeneous, occurring at defects such as grain boundaries, dislocations or foreign bodies such as non-metallic inclusions. In such cases an energetic advantage is obtained by eliminating a portion of the matrix/interface during nucleus formation.

1.3.2 Metastable Reconstructive Transformation in Steel

Metastable phases can be formed at the expense of the thermodynamically favoured phase if there is a suitable kinetic obstacle to the latter's formation. For example, a large activation energy for nucleation, or a slow growth process can inhibit the formation of the stable phase. In situations such as these, provided that there is sufficient thermodynamic driving force, metastable phases which can nucleate and grow at greater rates can form.

Considering the case of a plain carbon steel, the chemical potential of carbon and iron in ferrite of a given composition ($\overline{x}$) is given by the values of the intercept of a tangent line to the ferrite free energy curve at $\overline{x}$ with the free energy axis at $x = 0$ and $x = 1$ respectively. At a given temperature the compostitions of a two phase equilibrium mixture will be that which gives equal chemical potential to all components across the phase interface. This condition is represented by the case where two free energy curves have the same tangent line. For the decomposition of a supersaturated austenite into a two phase α/γ mixture as shown in Figure 1.4, the free energy change ΔG will be equal to the separation of the parent free energy curve at $\overline{x}$ and the line joining the product curves at their respective compositions x_α and x_γ. As Figure 1.4 shows, for a metastable transformation in which the modified ferrite curve is displaced along

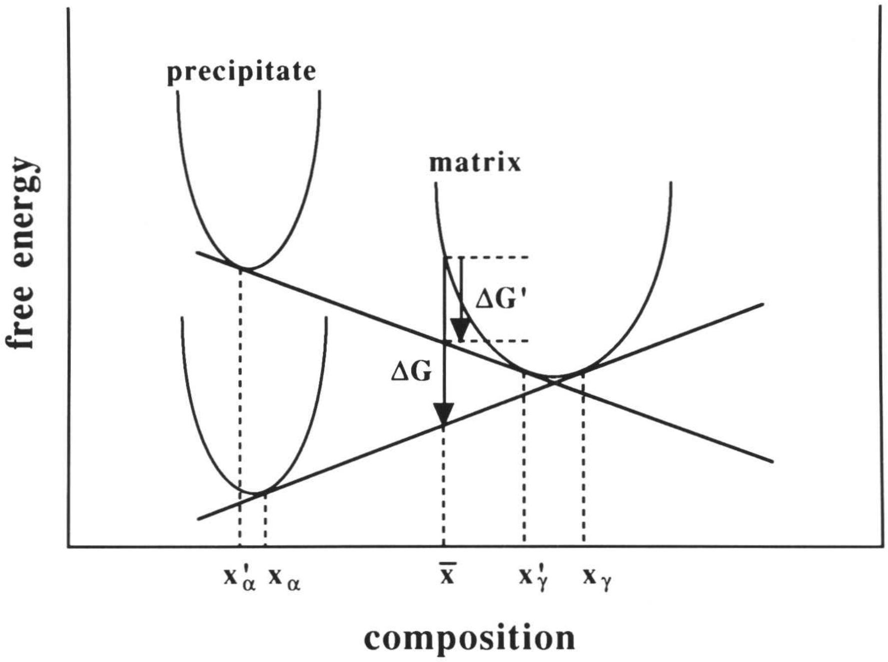

Figure 1.4 The free energy change on formation of a metastable phase showing the differences between the equilibrium and metastable equilibrium compositions

the free energy axis the magnitude of the free energy change $\Delta G'$ is reduced, and the tangent line touches the curves in new positions, indicating that the metastable equilibrium phase compositions differ from the equilibrium values. A characteristic of metastable transformations is that the composition of the matrix in metastable equilibrium with the precipitated phase lies closer to the bulk composition than does the equilibrium matrix composition. The importance of this fact will be explained later when considering the bainite transformation in steels.

Austenite

An example of metastable austenite formation is in steels where δ is the stable phase at high temperatures. Austenite can sometimes form directly from the liquid. This is especially true in welds if cooling rates are high and the solute partitioning coefficient is closer to unity for austenite than ferrite. The solute partitioning coefficient k is given by

$$k = x_s/x_l$$

where x_s and x_l refer to the solute mole fraction of the solidus and liquidus respectively.

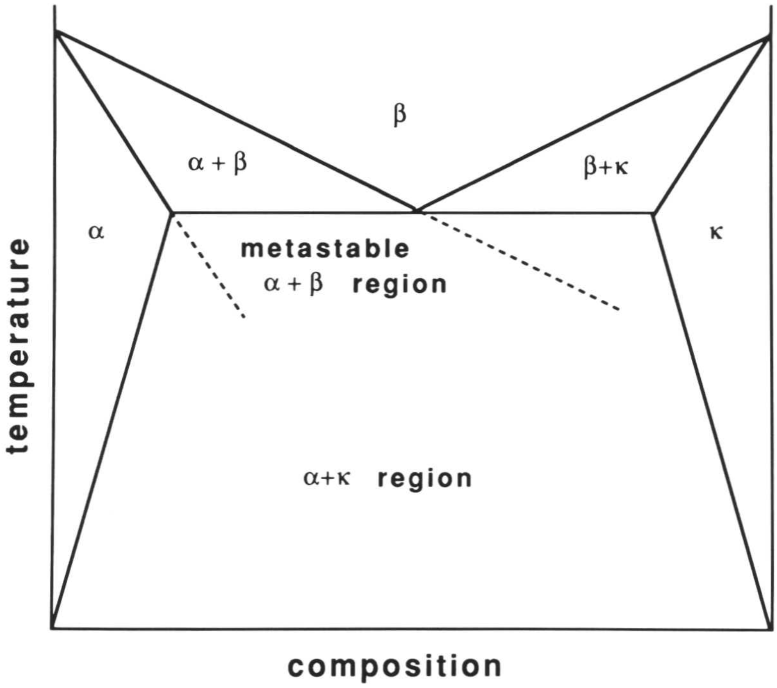

Figure 1.5 Extrapolation of the phase boundaries into regions of metastability

Ferrite

Another type of metastable transformation involves the formation of a phase outside the temperature or composition range for which it is the equilibrium phase. It may be that the growth rate of the metastable phase exceeds that of the equilibrium phase. As demonstrated by Figure 1.5 the phase boundaries can be extrapolated in such cases to give the metastable equilibrium phase compositions outside their normal range of stability.

A special kind of metastable transformation from austenite to ferrite can occur in alloy steels containing both substitutional and interstitial solutes. Let the interstitial solute be carbon, and let X represent the substitutional solute element. At the interface between the austenite and ferrite partitioning of the substitutional solute and carbon occurs. The velocity $V_{\rm int}$ of the interface must of such a value as to satisfy the flux equations for both solutes simultaneously *i.e.*

$$(c_1^{\gamma\alpha} - c_1^{\alpha\gamma})\, V_{\rm int} = D_{11} \nabla c_1$$

and

$$(c_2^{\gamma\alpha} - c_2^{\alpha\gamma})\, V_{\rm int} = D_{22} \nabla c_2$$

where c_1 and c_2 are the concentrations of carbon and X respectively, with D_{22} being the diffusion coefficient of the substitutional solute. The superscripts $\alpha\gamma$ and $\gamma\alpha$ denote the *interface* values of c_1 and c_2 in the ferrite and the austenite respectively. Because $D_{11} >> D_{22}$ the equilibrium values of the interface compositions will not satisfy the transport equations. Modified values are adopted, which can fall into one of two regimes, depending on the degree of austenite supersaturation.

Isothermal sections of a ternary phase diagram Fe–X–C are shown in Figure 1.6, where X is a substitutional alloying element. It is demonstrated in the diagram how the interface compositions are chosen so that the ferrite and austenite compositions are equilibrium–related, though they are not the equilibrium compositions for the alloy composition as a whole. In Figure 1.6 diagram (a) illustrates the case for small supersaturations. The austenite composition of the interface lies along the carbon isoactivity line, resulting in a very small activity gradient driving the diffusion of carbon, producing a small carbon flux. The activity gradient of X is steeper, and under these conditions appreciable partitioning of X is possible. In diagram (b) the case for high supersaturations is shown. The interface compositions are chosen this time to give the concentration of X in the ferrite very close to the value for the bulk alloy. This results in negligible partitioning of the substitutional solute, and hence its diffusion field can be very short, giving a sharp concentration spike at the interface. Under these conditions the interface can advance rapidly, and appreciable partitioning of carbon is possible.

In this way, two regimes are found, one in which there is considerable diffusion of carbon ahead of the interface but negligible partitioning of X, and one where there is only a shallow composition gradient of carbon ahead of the interface and the substitutional alloy element partitions over a larger range. These regimes are named 'Negligible Partitioning Local Equilibrium' or NPLE and 'Partitioning Local Equilibrium' or PLE respectively. In both cases there continuity of chemical potential across the interface.

At even faster growth rates it becomes impossible for the maintenance of equilibrium of the substitutional alloying elements. The transformation then proceeds without the partitioning of X at all, even at the interface. Free energy minimisation is then achieved with respect to carbon only, with the constraint that the Fe/X ratio is constant everywhere. This condition is known as paraequilibrium and is especially useful when considering the transformation of austenite to ferrite in steel welds.

1.3.3 Metastable Displacive Transformations in Steels

Thermodynamic equilibrium is usually attained by the diffusion of atoms into the lowest energy sites. For this process to occur requires sufficient atomic mobility for atoms to overcome the potential energy barrier surrounding their existing higher energy site. At lower temperatures this becomes increasingly difficult as the diffusivity decreases. The attainment of equilibrium then requires extremely slow cooling, usually at impractical rates. A mechanism which allows

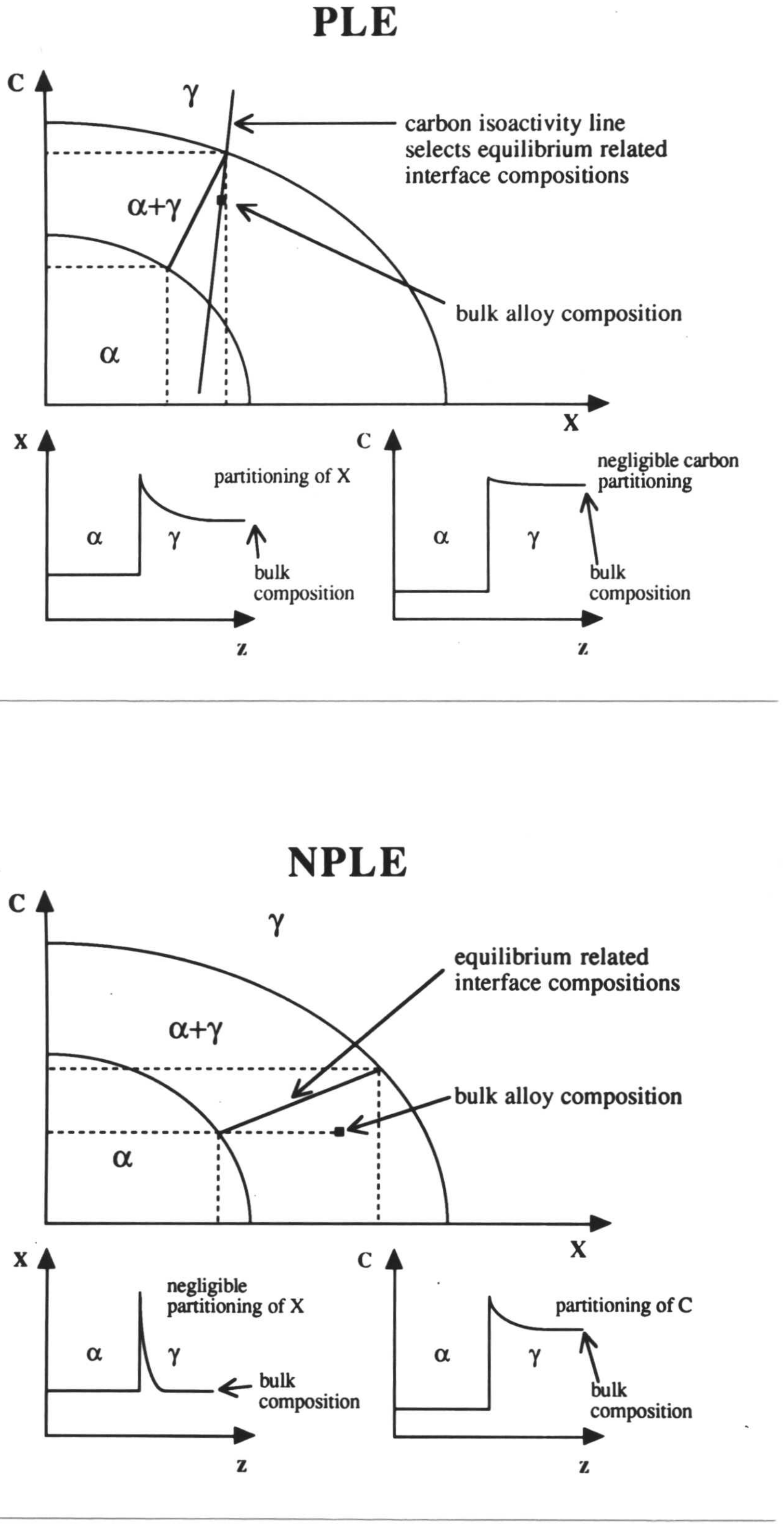

Figure 1.6 Ternary Fe–C–X phase diagrams demonstrating the regimes in which PLE and NPLE transformation can occur, and the choice of interface compositions

phase transformation without the need for diffusive jumps can under those circumstances have a kinetic advantage.

Figure 1.7 shows the mechanism by which the transformation from austenite to ferrite can be achieved without the need for atoms to move a distance as large as an inter-atomic spacing. Considering two unit cells of face centered cubic austenite γ as shown in Figure 1.7 a body centered tetragonal cell (bct) can be defined within the same structure. Representing the base vectors of the austenite cell as $\mathbf{a}_\gamma$, $\mathbf{b}_\gamma$ and $\mathbf{c}_\gamma$ and those of the new ferrite cell as $\mathbf{a}_{\mathrm{bct}}$, $\mathbf{b}_{\mathrm{bct}}$ and $\mathbf{c}_{\mathrm{bct}}$ the two cells can be related as follows

$$\mathbf{a}_{\mathrm{bct}} = \frac{1}{2}(\mathbf{a}_\gamma - \mathbf{b}_\gamma)$$

$$\mathbf{b}_{\mathrm{bct}} = \frac{1}{2}(\mathbf{a}_\gamma + \mathbf{b}_\gamma)$$

$$\mathbf{c}_{\mathrm{bct}} = \mathbf{c}_\gamma$$

Transformation is then accompanied by expansion along the $\mathbf{a}_{\mathrm{bct}}$ and $\mathbf{b}_{\mathrm{bct}}$ and contraction along $\mathbf{c}_{\mathrm{bct}}$ producing a cubic or a tetragonal ferrite lattice. This is known as the Bain Strain.

Diffusion is not necessary to achieve the change from fcc to bcc although it should be noted that additional deformation is required in order to ensure that the strain energy is minimised. Thus the *macroscopic* shape change is not in fact the one described by the Bain Strain, but is in fact an invariant plane strain (IPS).

Because of the large shear component of the IPS the ferrite, when it forms under constraint, has a large strain energy. If, at a given undercooling below Ae_3 there is enough driving force to overcome this strain energy then this mechanism becomes feasible.

Three forms of ferrite (with a fourth being an additional variant of one form) can grow by a displacive mechanism.

Widmanstätten Ferrite

The typical morphology of Widmanstätten ferrite is shown in Figure 1.8. Formation of this phase occurs at rather small undercoolings below Ae_3 (Bhadeshia, 1985). Upon transformation of polished specimens surface relief is observed, often doubly tilted, tent–like, but sometimes singly tilted, consistent with an invariant plane strain (Watson & McDougall, 1973). These observations led to the view that Widmanstätten ferrite grows by a displacive transformation. It was shown though that there was insufficient free energy for the formation of a single plate by such a mechanism at such low undercoolings below the Ae_3 temperature (Aaronson *et al.*, 1975). Transformation in fact involves the mutually accommodating growth of two plates back-to-back, minimising the strain energy of formation. The adjacent plates, illustrated in

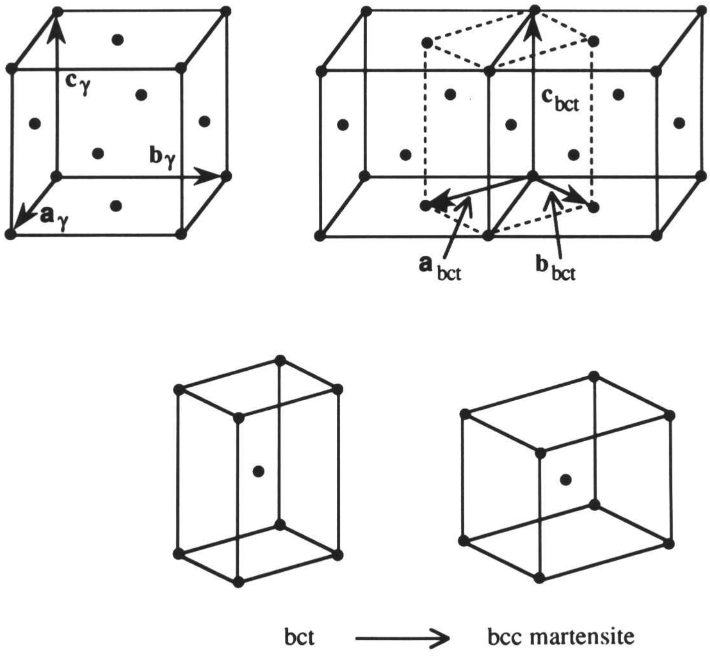

Figure 1.7 The Bain Strain lattice transformation

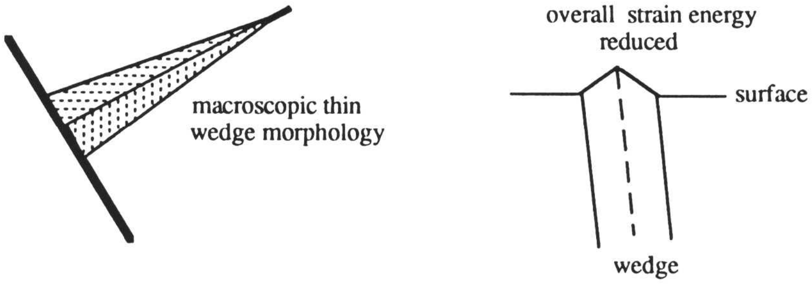

Figure 1.8 Typical Widmanstätten ferrite morphology

Figure 1.8, are found to be two closely related variants (Bhadeshia, 1980), each having a slightly different orientation relationship with the surrounding austenite. The effect of the mutual accommodation is to reduce elastic the distortion around the plates as is shown in Figure 1.8, thereby reducing the strain energy to about 50 J mol^{-1} (Bhadeshia, 1981a).

Widmanstätten ferrite grows under paraequilibrium conditions, the carbon partitioning occurring *during* transformation, whereas the substitutional lattice is merely displaced, with no substitutional solute partitioning. On an optical scale, a Widmanstätten ferrite plate has the appearance of a thin wedge which grows as the tip advances, the wedge shape being due to the slightly different interfacial orientation that the adjacent plates in the Widmanstätten ferrite wedge have with the austenite.

Bainite

Perhaps the most interesting of all the metastable transformations in steels is bainite. The mechanism of transformation has been difficult to elucidate and has been hotly debated. One school of thought maintains that bainite is the product of a reconstructive transformation, with the opposing side holding the view that transformation is displacive and diffusionless but that the decarburisation of ferrite occurs after transformation (Aaronson, 1962; Ko & Cottrell, 1952; Heheman, Kinsman & Aaronson, 1972; Kinsman, Eichen & Aaronson, 1975; Bhadeshia & Edmonds, 1979, 1980). A self-consistent picture has now emerged in which bainite is established as a shear transformation where formation involves the repeated nucleation and growth of platelets which form aggregates known collectively as sheaves, shown schematically in Figure 1.9. The appearance of a sheaf under optical microscopy is that of a thin wedge. With transmission electron microscopy the individual plates or sub-units within a sheaf become observable. Sheaves appear to grow by a lengthening and thickening process, which if fact results from the nucleation of further sub-units both at the tips of previously formed plates, and side by side with them. Nucleation at the plate tips is thought to be the more effective of the two processes, so it is not surprising to observe sheaves with an overall plate-like appearance (Bhadeshia & Christian, 1990).

Individual sub-units form with an initial full supersaturation of carbon (Bhadeshia & Edmonds, 1979, 1980). The ferrite then decarburises either by the diffusion of carbon into the surrounding untransformed austenite, and/or by precipitation of carbides within the ferrite. It is by these two decarburisation mechanisms that the two forms of classical bainite are distinguished. Carbon partitioning to the austenite leads to the formation of upper bainite, with its carbide-free ferrite plates. Precipitation of carbides within the ferrite leads to lower bainite. The time taken to decarburise by diffusion when compared to that required to precipitate carbides in ferrite is what distinguishes the two mechanisms (Takahashi & Bhadeshia, 1990).

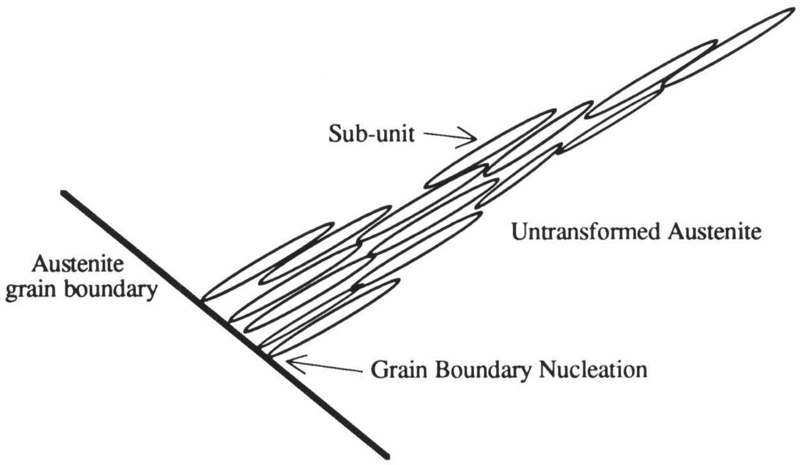

Figure 1.9 Schematic representation of a bainite sheaf.

At higher temperatures where decarburisation by diffusion is fast, upper bainite forms. The carbon enriched austenite then either decomposes to a ferrite/carbide aggregate, transforms to martensite or is retained as austenite, depending on the alloy composition and the transformation conditions. As the temperature decreases, the time to decarburise by diffusion increases until a threshold point is reached when carbide nucleation and growth can occur inside the ferrite within a shorter time interval. This is the mechanism that leads to lower bainite. Both mechanisms are illustrated in Figure 1.10.

Thermodynamic analysis of the conditions of formation has provided supportive evidence for the diffusionless reaction mechanism. Transformation is not observed when it becomes energetically impossible to form supersaturated bainitic ferrite with its associated strain energy of 400 J mol^{-1}. This thermodynamic condition can occur either because the undercooling below Ae_3 is insufficient, or because, as a result of prior ferrite formation, the carbon enrichment of the untransformed austenite has reached a level that reduces the free energy change of the γ/α transformation below the critical level. This latter condition leads to a phenomenon known as *incomplete reaction* where, at a given temperature, the volume fraction of bainite formed, as well as the austenite composition at reaction termination, is below the value predicted by equilibrium or paraequilibrium conditions. If the reaction were reconstructive in character then transformation would be expected to proceed until the austenite carbon content reached the

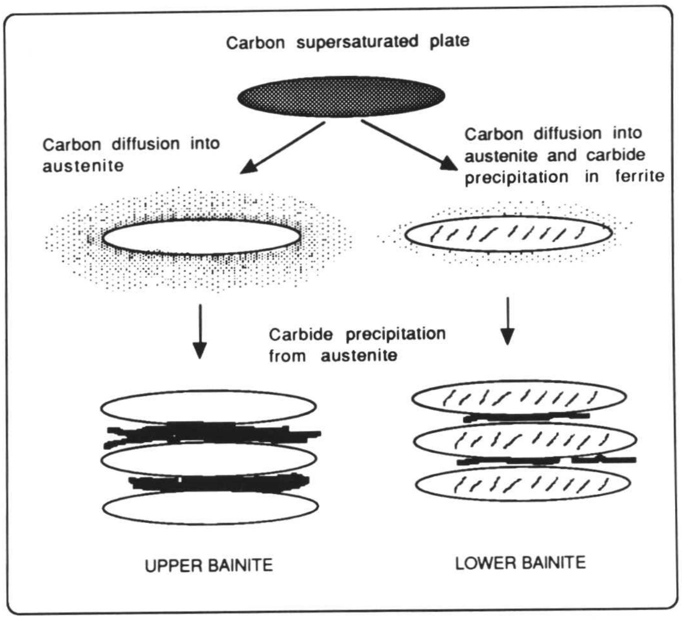

Figure 1.10 The development of carbides in upper and lower bainite

paraequilibrium Ae_3 boundary.

It can also be demonstrated that, even on the finest scale, there is no partitioning of substitutional alloying elements at the bainitic ferrite/austenite interface (Bhadeshia & Waugh, 1981).

Bainitic steels find great use in engineering because of their combination of toughness and strength. Bainitic weld metals are used extensively in the power generation industry because of its stable microstructure, conferring high temperature stability to the joint.

Acicular Ferrite

Acicular ferrite first came to prominence as a phase forming in weld deposits. Appearing to nucleate at non-metallic inclusions present in the weld pool (Ito & Nakanishi, 1976), the phase formed at intermediate temperatures, between that of allotriomorphic ferrite and martensite formation. The typical morphology of acicular ferrite is shown in Figure 1.11. Originally, it was speculated that acicular ferrite was a form of Widmanstätten ferrite (Ricks, Howell & Barrite, 1982), but it has recently become apparent that it is actually an intragranularly-nucleated form of bainite.

With its fine microstructure of disorganised plates it imparts good toughness and strength to weld metals and is therefore a highly desirable phase. By presenting a tortuous path to an

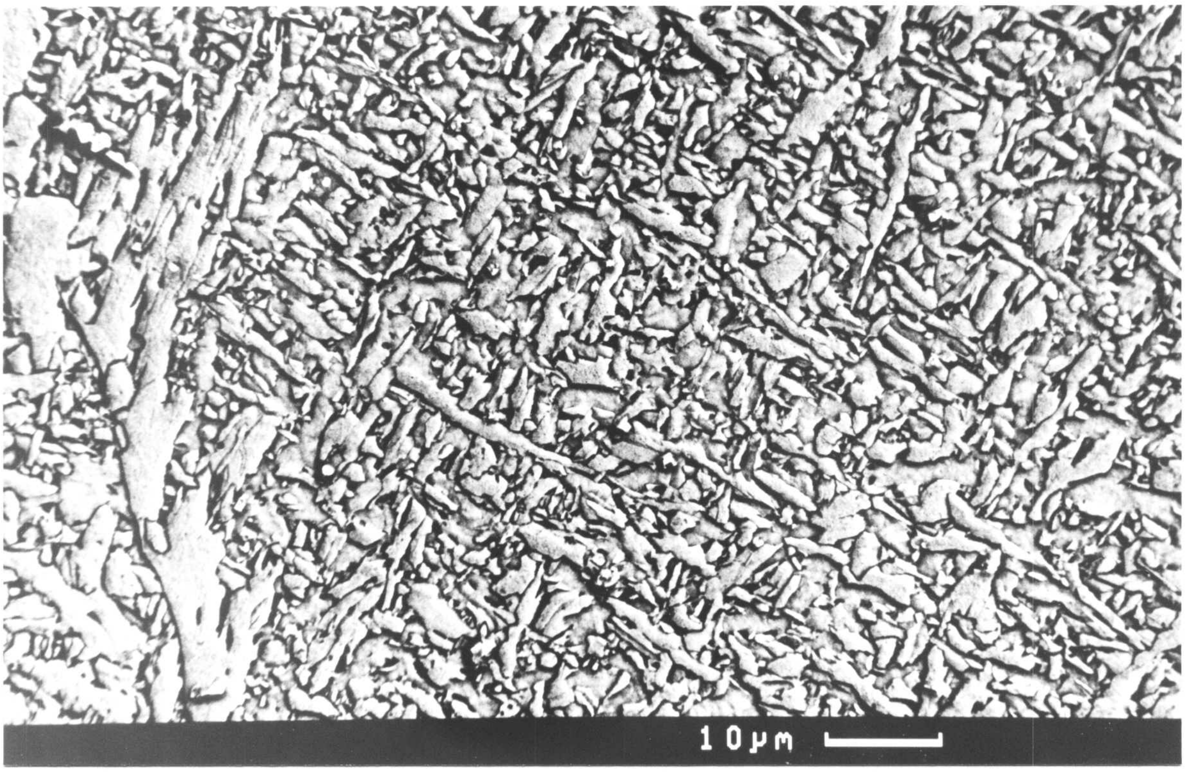

Figure 1.11 Morphology of Acicular Ferrite

advancing crack more energy is absorbed per unit of propogation, improving toughness (Ito & Nakanishi, 1982).

Weld deposits are notable for the very large, columnar prior austenite grains. These are a result of the high temperatures and large thermal gradients within the weld pool which undergoes cellular solidification to large δ grains, which then transform to the columnar γ grains. A large austenite grain size is one requirement for the stimulation of intragranular nucleation on inclusions since the number density of competing grain boundary nucleation sites is then relatively decreased. This has been confirmed by studying the transformation behaviour of reheated weld metals. It is found that after austenitising at low temperatures, the small γ-grained specimens transform to bainite. Under the same conditions, high temperature austenitisation, and the accompanying large austenite grains, gives a predominantly acicular ferrite microstructure (Yang & Bhadeshia, 1987). Acicular ferrite also shows a transformation surface relief consistent with an IPS shape change (Strangwood & Bhadeshia, 1987) and an incomplete reaction, similar to bainite (Yang & Bhadeshia, 1987). As well as these similarities, it has been demonstrated that in the same way that upper or lower bainite are found in wrought steels, upper and lower acicular ferrite can be generated by altering the weld chemistry (Sugden & Bhadeshia, 1989). However, lower acicular ferrite is not normally observed in real welds, since weld metal carbon concentrations are usually kept low in order to avoid the formation of brittle, high-carbon martensite.

It appears then, that acicular ferrite is identical to bainite, but nucleated on inclusions. The acicular ferrite plates do not normally cluster as sheaves, presumably because the hard impingement of plates with those nucleated on neighbouring sites makes the development of a sheaf impossible. It is common to see plates nucleating autocatalytically *i.e.* plate nucleation on previously transformed regions. In this manner the number of sites for nucleation increases as transformation proceeds – this is the essence of autocatalysis. It is not yet known whether nucleation is aided by the stress field around the plate, by the dislocations that form in the austenite as a result of the plastic accommodation of the plate's shape change, or whether existing plates simply provide a surface for heterogeneous nucleation.

Thermodynamics of Widmanstätten Ferrite and Bainite Nucleation

Bainite and Widmanstätten ferrite are displacive transformations which form at relatively small undercoolings, above the temperature at which nucleation can occur by a displacive diffusionless process (*i.e.* the M_S temperature, at which martensite occurs). The nucleating mechanism for these reactions must therefore be slightly different to that of martensite and this difference is the essence of the problem of rationalising the transformations in steels.

Isothermal transformation diagrams in steels show the regimes in which reconstructive and displacive reactions occur. In lightly alloyed steels the temperature ranges over which the different reaction mechanisms operate often overlap giving the overall appearance of a single C–curve. Increasing the substitutional solute content of the steel clarifies the picture by separating the reconstructive and displacive transformation ranges so that each mechanism has a separate C–curve. As the alloy content is increased the lower C–curve develops a flat top indicating that the nucleation of ferrite decreases very rapidly over a very narrow range of temperature increase.

The work of Steven and Haynes (1956) provides a rich dataset for the highest temperature T_H in the lower C-curve of TTT diagrams. Depending on the alloy content of these steels T_H can correspond to the formation of either bainite or Widmanstätten ferrite. The data were used to investigate the relationship between the free energy change and the temperature at which formation became possible (Bhadeshia, 1981a).

Nucleation theory states that for the formation of a very small amount of precipitate the composition change in the matrix is negligible, therefore the most likely precipitate composition is that which allows the maximum free energy change under these conditions (Hillert, 1953). This change is termed ΔG_m and is discussed in detail in section *2.1.2*.

Bhadeshia plotted the values of $\Delta G_m \{T_H\}$ against T_H. As is shown in Figure 1.12 the results regress onto a single straight line. The implications of this result are that

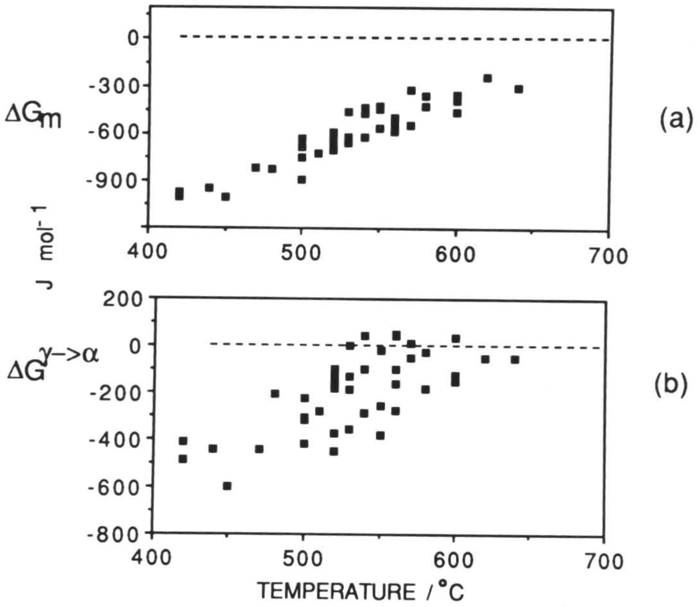

Figure 1.12 Comparison plots of the relationship between ΔG_m and the free energy change for no composition change $\Delta G^{\gamma \to \alpha'}$ against the highest temperature for displacive nucleation.

a) Since a single line is found to represent all the data, Widmanstätten ferrite and bainite must develop from the same nucleus, but the phase into which the nucleus eventually develops must depend on the conditions during growth.

b) The linear relationship indicates (as shown later) that the activation energy nucleation is linearly dependent on the ΔG_m.

c) Carbon partitioning occurs during the nucleation process. This is the essential difference between the nucleation of Widmanstätten ferrite and bainite and that of martensite (discussed in detail in section *2.1.5*).

These findings can be rationalised if it considered that at T_H (the temperature at which displacive nucleation is first possible) there is a constant nucleation rate N

$$N \propto \nu \exp\left\{-\frac{G^*}{RT}\right\}$$

where ν is the attempt frequency, G^* is the activation energy.

In order to obtain an expression for the relationship between the activation energy for nucleation and the free energy change at T_H consider that

$$G^*\{T_H\} \propto \beta T_H$$

it is desired to find

$$G^*\{T_H\} = f\{G_m\{T_H\}\}$$

hence

$$\beta T_H = f\{G_m\{T_H\}\}$$

When Bhadeshia plotted $G_m\{T_H\}$ versus T_H he obtained a linear relationship, which implies

$$T_H = mG_m\{T_H\} + c$$

where m and c are constants. This in turn implies

$$G^* = m'G_m\{T_H\} + c'$$

This result is consistent with the theoretical expression for the activation energy when 'nucleation' is by a displacive mechansim involving the growth of pre-existing embryos (Olson & Cohen, 1976).

Martensite

The only truly diffusionless transformation forming in steel, martensite occurs when there is sufficient thermodynamic driving force to both nucleate and grow displacively without any need for carbon diffusion.

Martensite forms as plates which can propagate right across austenite grains, though they are never observed to cross the grain boundaries. Between the plates it is common to see thin layers of retained austenite. The shape change produces characteristic surface relief consistent with a macroscopic invariant-plane strain deformation. Carbon within the austenite as it transforms remains in solution in the martensite, the diffusion velocity at the transformation temperature being small in comparison to the growth velocity.

By holding a martensitic structure at higher temperatures, carbide precipitation is encouraged. This process (tempering) relieves some of the strain due to the distorsions around the carbon atoms in the martensite. It is possible for some low alloy steels to autotemper *i.e.* the martensite is almost instantly tempered as the transformation proceeds.

The nucleation of martensite is believed to occur when a suitable coherent fault in the austenite matrix is induced to grow, by the propogation of the interface dislocations, under the stress provided by the chemical free energy change. It is expected that a variety of suitable faults are present in austenite *e.g.* at grain boundaries. Each fault requires a different driving force in order to activate it and hence there is a distribution of fault potency. This fact is significant when considering steels that transform with burst characteristics *i.e.* with a very large autocatalytic effect. With such steels, at a given temperature only those faults with a low enough activation energy can form nuclei, and these then initiate a certain degree of transformation. It is necessary to lower the temperature, thereby increasing the driving force and stimulating less potent faults to induce further nucleation and hence increase the fraction of martensite. In this manner martensite shows athermal characteristics. It is possible however for isothermal martensite formation to occur in some steels (Olson & Cohen, 1976).

1.4 Development of Microstructure During the Cooling of Weld Metal.

1.4.1 Solidification

In general low alloy steel welds solidify as δ ferrite. Growth of this phase is epitaxial from the base plate grains at the fusion boundary for low alloy steels (Davies & Garland, 1975).

Transformation to δ ferrite occurs with a cellular δ/liquid front (Calvo *et al.* 1963). Since near the fusion boundary the base plate grains are coarsened by the high temperatures this gives rise to a δ ferrite grain cross section much larger than that of the original plate.

Under certain conditions of high cooling rate it is possible for the steels to solidify directly as metastable γ. This is especially true in cases where the solute partitioning coefficient for the austenite is closer to unity than that of ferrite (Fredriksson, 1976, 1983), in which case the growth rate of austenite may exceed that of the ferrite. It is also possible for highly alloyed steels to have austenite as the stable high temperature phase, and consequently solidify as γ.

The diffusivity of substitutional solute elements is generally higher in ferrite than in austenite, enabling segregation effects to be minimised (Fredriksson, 1976, 1983). Any segregated regions are found at the δ/δ boundaries. Non–metallic inclusions tend to gather at solidification cell boundaries. Subsequent transformation to austenite then brings these inclusions into the centre of the grains where they can play an important role in nucleating other phases (Sugden & Bhadeshia, 1988). The preferential presence of inclusions at austenite boundaries would, on the other hand, incorporate them within the allotriomorphic ferrite which forms at lower temperature. This phase is relatively brittle at best, without the detrimental presence of inclusions. In these ways then it is apparent that solidification as δ ferrite is desirable.

At any given point during welding, the moving heat source causes a variation of temperature with time. Grain solidification generally occurs along the direction of maximum heat flow *i.e.* down the steepest thermal gradient. However, as the temperature gradient also changes with time, the austenite grains which evolve from the δ tend to curve away from the δ boundaries where they first nucleated (Dadian, 1986). It is by this process that segregated regions and inclusions, previously at δ boundaries, are incorporated into the body of the austenite grains. This is shown schematically in Figure 1.13.

Since the nucleation and growth of austenite occurs at the δ–ferrite boundaries the austenite grain size is in general smaller that of the δ–ferrite. The situation might change if the austenite grains coarsen during cooling. To some extent the eventual γ grain size is influenced by the the plate grain size because of the epitaxial solidification. The degree of coarsening of the hot base plate grains at the fusion line is therefore important in this context. The eventual size of the γ grains does have a profound effect on subsequent transformations occurring in the cooling weld metal (Bhadeshia, Svensson & Gretoft, 1985).

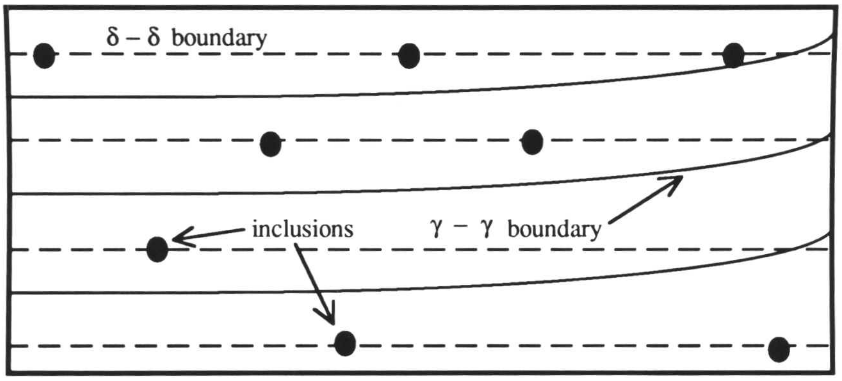

Figure 1.13 Schematic representation of the relative growth orientations of δ and γ grains

Allotriomorphic ferrite begins to form when the weld metal cools below the Ae_3 temperature. In most cases, because of the high cooling rates in welds, growth occurs under paraequilibrium conditions (Bhadeshia *et al.* 1985), with no redistribution of substitutional solute atoms, though NPLE and PLE growth can occur. Nucleation occurs heterogeneously at the austenite grain boundaries, and because of the energetic benefits of doing so, growth along these boundaries is fast, decorating the austenite grains (Bhadeshia, 1991). When a uniform polycrystalline layer of ferrite has been formed, covering all the austenite boundary surface, growth can only proceed into the grain. It has been shown that the thickness of allotriomorphic ferrite formed is insensitive to austenite grain size suggesting that nucleation is not the dominant factor in determining the transformation kinetics of allotriomorphic ferrite (Dallum & Olson, 1989).

Nucleation at a γ/γ boundary means that the ferrite is in contact with two differently oriented austenite grains. The resulting difference in crystallographic orientation between the ferrite and the two austenite grains manifests itself in the interface and growth characteristics. As a rule, there will be a side with good matching of close packed directions and planes and there will be a poorly matched side with and incoherent interface. On the well matched side the interface will propagate by the movement of incoherent ledges on the well matched interface, parallel to it. On the poorly matched side growth is by movement of the incoherent interface normal to itself.

Under paraequilibrium conditions growth is carbon diffusion-controlled. For a fully decorated austenite grain the ferrite allotriomorph growth can then be treated as a one–dimensional diffusion–controlled thickening.

As the temperature decreases transformations by diffusional processes become sluggish, and once displacive transformations are thermodynamically feasible, they can dominate. The first displacive reaction to occur is Widmanstätten ferrite formation. This phase can nucleate directly on the γ/γ boundary or on the newly formed allotriomorphs. These two kinds of Widmanstätten ferrite are called primary and secondary Widmanstätten ferrite respectively. With the appearance of a thin wedge, though actually two mutually accommodating plates, growing rapidly in the direction parallel to its length, plates can grow right across austenite grains in a matter of seconds unless impingement with intragranularly nucleated products stifles growth.

The intragranular nucleation product mentioned above refers to acicular ferrite, which forms in the same temperature range as bainite does in wrought steels. Investigation has led to the identification of acicular ferrite as a variant of bainite but nucleated on inclusions within the austenite grains.

Depending on alloy composition and cooling rate, acicular ferrite can form after allotriomorphic ferrite formation has occurred on the γ/γ boundaries or before this transformation has had an opportunity to begin (*e.g.* in high strength welds). In the case of some steels in which transformation kinetics are fast, research suggests that the presence of allotriomorphic ferrite is essential in order to suppress the nucleation and rapid dominance of bainite at these boundaries (Babu & Bhadeshia, 1991).

Following the acicular ferrite transformation, the remaining austenite can form a variety of 'microphases'. This term refers to martensite, pearlite or retained austenite. The grouping of the acicular ferrite and microphases together, as is done in some welding research papers loses its meaning when considering high strength welds which consist entirely of acicular ferrite and martensite (Bhadeshia & Svensson, 1988). Allotriomorphic ferrite, Widmanstätten ferrite and acicular ferrite are shown together in a weld microstructure in Figure 1.14.

The Role of Inclusions in Microstructure Development

As a result of the deoxidation reactions at high temperatures within the weld pool, particles of non-metallic compounds that do not separate into the slag layer become trapped in the solidifying steel.

During solidification to δ ferrite the inclusions are swept to the δ/δ boundary regions of the cellular front as it progresses. The resulting alignment of the inclusion particles is retained

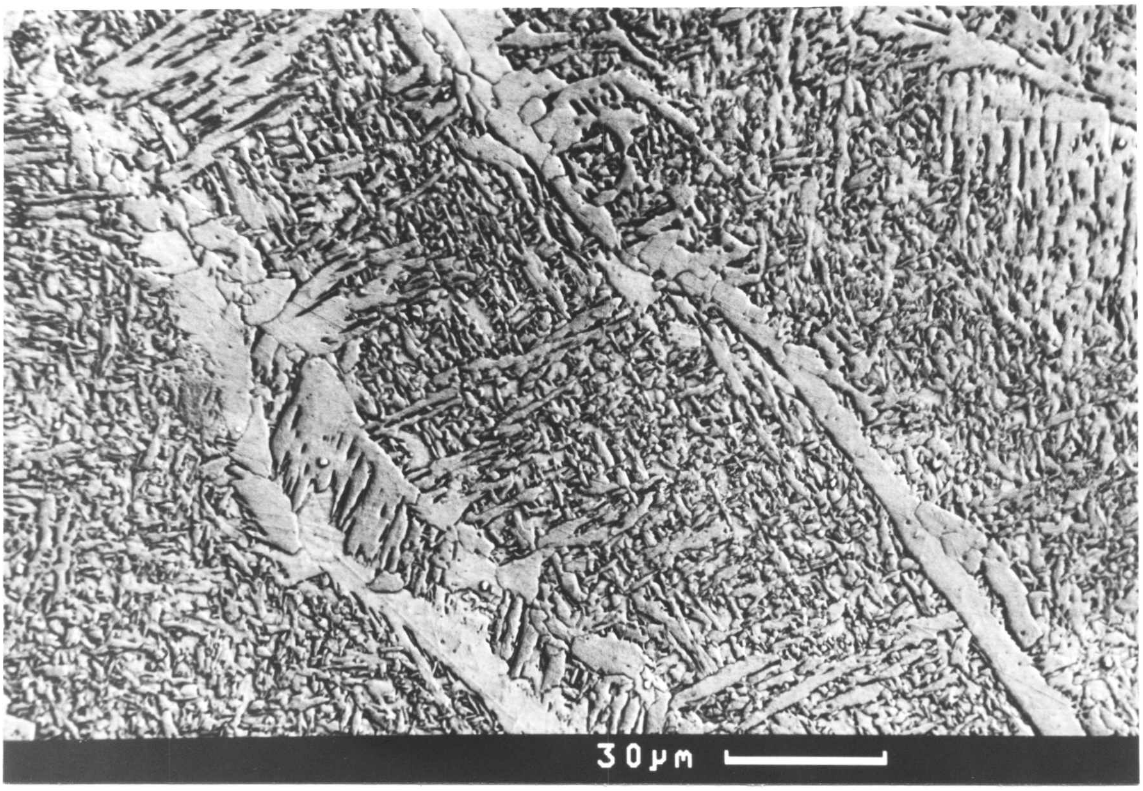

Figure 1.14 The morphology of allotriomorphic ferrite α, Widmanstätten ferrite α_W and acicular ferrite α_a in a weld deposit

to room temperature even though austenite formation means that the particles are no longer located at grain boundaries in the final microstructure.

In general the presence of foreign bodies in the weld metal affects its homogeneity, which is a crucial factor in determining physical properties. Inclusions in particular act as stress raisers, increasing the chances of crack initiation. However, they are also the sites for the intragranular nucleation of acicular ferrite which is beneficial to weld properties.

It has been shown that in order to optimise their nucleating properties the inclusions must (a) be of the correct chemical composition; (b) be present in sufficient numbers; and (c) have the correct size distribution (Grong & Matlock, 1986).

The exact nature of nucleation at the inclusion surface is not known. It has been found that inclusions having the greatest difference in thermal expansion coefficient with austenite are the most effective nucleants. Also postulated is that nucleating effect might be attributed to (a) the presence of dislocations formed by deformation of the austenite driven by the differential thermal contraction at the inclusion/matrix interface; (b) the interaction of transformation strain of the acicular ferrite particle with the stress field around the inclusion; (c) the presence of the inclusion as an inert heterogeneous nucleation site (Farrar & Harrison, 1987). Chemical reactions at the ferrite/inclusion interface are also possible (Strangwood & Bhadeshia, 1987;

Gregg, 1992).

1.5 An Outline of the Weld Fusion Zone Microstructure Model

Utilising phase transformations theory, combined with experimental data, a semi-empirical model has been developed by Bhadeshia and co-workers over recent years, that is capable of some remarkably accurate predictions of weld microstructure.

From the chemical composition of the weld metal its phase diagram and TTT diagram can be calculated. From the welding variables such as process type, heat input and interpass temperature, the cooling behaviour of the weld can be estimated. Combination of isothermal transformation diagrams and cooling curve enables the volume fraction of the phases forming as the weld cools to be calculated

The sequence of reactions in the cooling weld is modelled as follows. Solidification is considered to occur as δ ferrite, and by considering the solute partitioning coefficient k between the ferrite and the liquid at the liquidus temperature the extent of solute segregation at room temperature can be estimated since there is little chance for homogenisation during cooling. Hence the composition of the segregated regions with respect to the element i is $k_i x_i$ (Gretoft *et al.* 1986).

It is not possible to estimated the austenite grain size that forms from the ferrite from fundamental theory and so a crude estimation of the transverse mean linear intercept $\overline{L}$ with the grain structure is made by the use of a regression equation.

$$\overline{\mathrm{L}}(\mu\mathrm{m}) = 64.5 - 445.8(\mathrm{wt\%C}) - 139(\mathrm{wt\%Si}) - 7.6(\mathrm{wt\%Mn}) + 16(\mathrm{heat\ \ input\ \ kJ\ mm^{-1}})$$

The first phase to form from the austenite is allotriomorphic ferrite. Transformation is assumed to begin when the Scheil approximation sum, applied to the calculated TTT diagram for the solute depleted regions, reaches unity. The time and temperature of this event are designated t_h and T_h respectively. Since boundary decoration by allotriomorphic ferrite is fast compared to growth normal to the interface, the transformation can be approximated as one dimensional carbon controlled growth, and paraequilibrium applies under the fast cooling conditions. The allotriomorph thickness q integrated over the temperature range T_h to T_l is

$$q = \int_{T_h}^{T_l} \left(0.5\alpha_1 t^{-1/2}\right) dt$$

where T_l represents the temperature at which the diffusional and displacive TTT curves cross, t_l being the time at which this happens. The value of α_1 is obtained by solving the equation

$$\frac{2\left(\underline{D_{11}}/\pi\right)^{1/2}(x^{\gamma\alpha} - \overline{x})}{x^{\gamma\alpha} - x^{\alpha\gamma}} = \alpha_1 \exp\left\{\frac{\alpha_1^2}{4\underline{D_{11}}}\right\} \mathrm{erfc}\left\{\frac{\alpha_1}{2\underline{D_{11}}^{1/2}}\right\}$$

which relates the mass of partitioned carbon from ferrite to that in the diffusion field ahead of the advancing interface. It is suggested that the major effect of alloying elements on weld metal transformation characteristics is by their effect and the kinetics of allotriomorphic ferrite formation.

The geometry of the grain structure, approximated by hexagonal prisms, relates the volume fraction of allotriomorphic ferrite to the allotriomorph thickness q.

$$V_\alpha = \frac{(2q\tan\{30°\}\,(2a - 2q\tan\{30°\}))}{a^2}$$

where a is the hexagonal austenite grain side length.

The next phase to form is Widmanstätten ferrite. The lengthening rate G of the plates is constant and can be estimated using the Trivedi theory of pate growth. If growth occurs for a time t_2 then the fraction of Widmanstätten ferrite growing from the austenite grain boundary, which may, or may not be covered with allotriomorphic ferrite is

$$V_{\alpha w} = C_4 G\left(\frac{2a - 4q\tan\{30°\}}{2a}\right) t_2^2$$

where the presence of q indicates the effect of previously formed allotriomorphic ferrite on the available volume for Widmanstätten ferrite growth. An important factor in determining the volume fraction of this phase is the term t_2. If the plate can grow unhindered across and austenite grain in time t_g then t_2 equals this time. If impingement with intragranularly nucleated acicular ferrite occurs after t_c and $t_c < t_g$ then t_2 will equal t_c. It is not possible to evaluate t_c from fundamental principles and so an empirically determined time of 2.011 s is used.

The final microstructural component to be estimated is acicular ferrite which is deduced by difference

$$V_{\alpha_a} = 1 - V_\alpha - V_{\alpha w} - V_m$$

The volume fraction of microphases V_m can be estimated thermodynamically by equating it to the volume fraction of untransformed austenite given by the paraequilibrium phase diagram, at the M_S temperature.

The microstructure model also predicts the effect of trace elements such as boron on the transformation behaviour of the steel, as well as predicting the chemistry of the non–metallic inclusions in the weld by considering the relative stability of the various inclusion phases that can form, given the composition of the steel.

Attempts have been made to model the relationship between microstructure and properties of welds. This process involves accounting for the solid solution as well as the microstructural strengthening effect of the various alloying elements and has met with reasonable success (Sugden, 1988). It is also of great importance to account for the scatter in toughness seen in weld deposits. This is accounted for in a novel way by considering the cause of such scatter to be the microstructural inhomogeneity of the weld resulting from the presence of more than one phase (Sugden & Bhadeshia, 1989). To refer to this inhomogeneity as entropy is however a mistake, since inhomogeneity implies a low entropy condition.

CHAPTER 2

Mathematical Modelling of Phase Transformations

2.1 Mathematical Modelling of Phase Transformations

The first step in modelling phase transitions in steels is to represent the chemical potential changes occurring in the austenite and ferrite phases as a function of carbon concentration and temperature. For the modelling of paraequilibrium transformation, other alloying elements can be accounted for by their effect on the transitions in pure iron. The free energy of ferrite at temperature T, carbon mole fraction x^α is

$$G^\alpha = x^\alpha \left(\mu_C^0 + RT \ln \{a_C^\alpha\}\right) + (1 - x^\alpha) \left(\mu_{Fe}^{\alpha 0} + RT \ln \{a_{Fe}^\alpha\}\right) \tag{2.1}$$

where a_C^α and a_{Fe}^α refer to the activity of carbon and iron, respectively, in the ferrite. The term μ_C^0 and $\mu_{Fe}^{\alpha 0}$ refer to the chemical potentials of graphite and of pure ferritic iron.
Using analogous notation, the free energy of austenite of carbon mole fraction x^γ is

$$G^\gamma = x^\gamma \left(\mu_C^0 + RT \ln \{a_C^\gamma\}\right) + (1 - x^\gamma) \left(\mu_{Fe}^{\gamma 0} + RT \ln \{a_{Fe}^\gamma\}\right) \tag{2.2}$$

The activities of carbon and iron in ferrite and austenite are themselves functions of the carbon mole fraction. These quantities can be estimated by use of the statistical thermodynamic theory of Lacher (1937) and Fowler & Guggenheim (1939).

Considering the ferrite phase, the activity of carbon is

$$\ln a_C^\alpha\{x^\alpha\} = 4 \ln \left[\frac{(9 - 6(2J_\alpha + 3)x^\alpha + (9 + 16J_\alpha)(x^\alpha)^2)^{1/2} - 3 + 5x^\alpha}{(9 - 6(2J_\alpha + 3)x^\alpha + (9 + 16J_\alpha)(x^\alpha)^2)^{1/2} + 3 - 5x^\alpha} \right]$$

$$+3 \ln \left[\frac{3 - 4x^\alpha}{x^\alpha} \right] + \frac{4w_\alpha}{RT} + \frac{\Delta \overline{H}_\alpha - \Delta \overline{S}_\alpha T}{RT} \tag{2.3}$$

where J_α is given by

$$J_\alpha = 1 - \exp\left(\frac{-w_\alpha}{RT}\right) \tag{2.4}$$

where w_α is the carbon-carbon interaction energy for ferrite and the terms $\Delta \overline{H}_\alpha$ and $\Delta \overline{S}_\alpha$ are the partial molar enthalpy and non-configurational entropy for solid solution of carbon in ferrite. By applying the Gibbs-Duhem relationship to the expression for the activity of carbon, the activity of iron can also be determined for ferrite. This gives (Hsu & Mou Yiwen, 1984), using analogous notation to the expression for ferrite

$$\ln a_{Fe}^\alpha\{x^\alpha\} = +9 \ln \left[\frac{3(1 - x^\alpha)}{(3 - 4x^\alpha)} \right]$$

$$+12\ln\left[\frac{3(1-2J_\alpha)+(8J_\alpha-3)x^\alpha-(9-6(2J_\alpha+3)x^\alpha+(9+16J_\alpha)(x^\alpha)^2)^{1/2}}{2J_\alpha(4x^\alpha-3)}\right] \tag{2.5}$$

In the austenite phase the activity of carbon is given by

$$\ln a_C^\gamma\{x^\gamma\}=6\ln\left[\frac{(1-2(1+2J_\gamma)x^\gamma+(1+8J_\gamma)(x^\gamma)^2)^{1/2}-1+3x^\gamma}{(1-2(1+2J_\gamma)x^\gamma+(1+8J_\gamma)(x^\gamma)^2)^{1/2}+1-3x^\gamma}\right]$$

$$+5\ln\left[\frac{1-2x^\gamma}{x^\gamma}\right]+\frac{6w_\gamma}{RT}+\frac{\Delta\overline{H}_\gamma-\Delta\overline{S}_\gamma T}{RT} \tag{2.6}$$

where

$$J_\gamma=1-\exp\left(\frac{-w_\gamma}{RT}\right) \tag{2.7}$$

The activity of iron austenite is then given by

$$\ln a_{Fe}^\gamma\{x^\gamma\}=6\ln\left[\frac{1-2J_\gamma+(4J_\gamma-1)-(1-2(1+2J_\gamma)x^\gamma+(1+8J_\gamma)(x^\gamma)^2)^{1/2}}{2J_\gamma(2x^\gamma-1)}\right]$$

$$+5\ln\left[\frac{1-x^\gamma}{1-2x^\gamma}\right] \tag{2.8}$$

The thermodynamic data for w_γ, $\Delta\overline{H}_\alpha$ and $\Delta\overline{H}_\gamma$ can be found in the work of Shiflet *et al.* (1978). $\Delta\overline{S}_\alpha$ and $\Delta\overline{S}_\gamma$ is taken from Lobo *et al.* (1976). The value of w_α was obtained by Bhadeshia (1980).

2.1.1 The $\gamma \rightarrow \gamma_1+\alpha$ Transformation

For the transition of austenite to the equilibrium $\alpha + \gamma$ phase mixture, the free energy change $\Delta G^{\gamma\rightarrow\gamma_1+\alpha}$ is shown diagrammatically in Figure 2.1. The equilibrium ferrite and austenite compositions are $x^{\alpha\gamma}$ and $x^{\gamma\alpha}$ respectively. The value of the free energy change is given by the expression

$$\begin{aligned}\Delta G^{\gamma\rightarrow\gamma_1+\alpha} &= vG^\alpha\{T,x^{\alpha\gamma}\}+(1-v)G^\gamma\{T,x^{\gamma\alpha}\}-G^\gamma\{T,\overline{x}\}\\ &= v\left(x^{\alpha\gamma}\left(\mu_C^0+RT\ln\{a_C^\alpha|_{x^{\alpha\gamma}}\}\right)+(1-x^{\alpha\gamma})\left(\mu_{Fe}^{\alpha\,0}+RT\ln\{a_{Fe}^\alpha|_{x^{\alpha\gamma}}\}\right)\right)\\ &+(1-v)\left(x^{\gamma\alpha}\left(\mu_C^0+RT\ln\{a_C^\gamma|_{x^{\gamma\alpha}}\}\right)+(1-x^{\gamma\alpha})\left(\mu_{Fe}^{\gamma\,0}+RT\ln\{a_{Fe}^\gamma|_{x^{\gamma\alpha}}\}\right)\right)\\ &-\overline{x}\left(\mu_C^0+RT\ln\{a_C^\gamma|_{\overline{x}}\}\right)+(1-\overline{x})\left(RT\ln\{a_{Fe}^\gamma|_{\overline{x}}\}\right)\end{aligned} \tag{2.9}$$

where

$$v=\frac{\overline{x}-x^{\gamma\alpha}}{x^{\alpha\gamma}-x^{\gamma\alpha}} \tag{2.10}$$

$a_{Fe}^\alpha|_{x^{\alpha\gamma}}$ and $a_C^\alpha|_{x^{\alpha\gamma}}$ denote the activities of carbon and iron in ferrite of composition $x^{\alpha\gamma}$ respectively. The activities of carbon and iron in austenite at composition $x^{\gamma\alpha}$ are expressed as

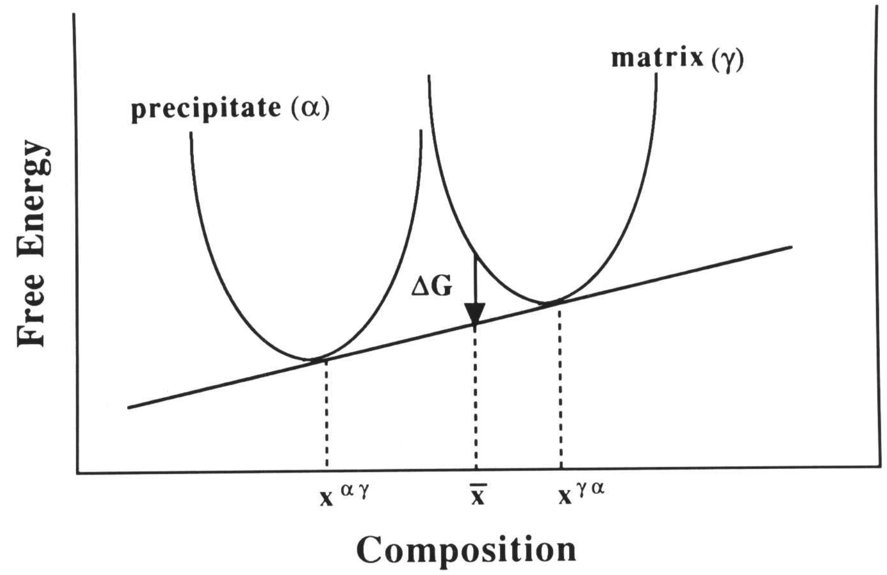

Figure 2.1 Free energy change on decomposition of austenite into a two–phase α/γ mixture of equilibrium composition.

$a^{\gamma}_{C}|_{x^{\gamma\alpha}}$ and $a^{\gamma}_{Fe}|_{x^{\gamma\alpha}}$. For austenite of bulk alloy composition the activities of carbon and iron are expressed as $a^{\gamma}_{C}|_{\overline{x}}$ and $a^{\gamma}_{Fe}|_{\overline{x}}$. The resulting free energy change is

$$\begin{aligned}\Delta G^{\gamma\rightarrow\gamma_1+\alpha} = {} & \left(\mu^{\alpha\,0}_{Fe} - \mu^{\gamma\,0}_{Fe}\right) + RTv\left(x^{\alpha\gamma}\ln\{a^{\alpha}_{C}|_{x^{\alpha\gamma}}\} + (1-x^{\alpha\gamma})\ln\{a^{\alpha}_{Fe}|_{x^{\alpha\gamma}}\}\right) \\ & + RT\,(1-v)\left(x^{\gamma\alpha}\ln\{a^{\gamma}_{C}|_{x^{\gamma\alpha}}\} + (1-x^{\gamma\alpha})\ln\{a^{\gamma}_{Fe}|_{x^{\gamma\alpha}}\}\right) \\ & - RT\,(1-v)\left(\overline{x}\ln\{a^{\gamma}_{C}|_{\overline{x}}\} + (1-\overline{x})\ln\{a^{\gamma}_{Fe}|_{\overline{x}}\}\right) \qquad (2.11)\end{aligned}$$

This value can then be calculated by substituting in the activity expressions $a^{\alpha}_{C}|_{x^{\alpha\gamma}}$, $a^{\alpha}_{Fe}|_{x^{\alpha\gamma}}$, $a^{\gamma}_{C}|_{x^{\gamma\alpha}}$, $a^{\gamma}_{Fe}|_{x^{\gamma\alpha}}$, $a^{\gamma}_{C}|_{\overline{x}}$, $a^{\gamma}_{Fe}|_{\overline{x}}$.

2.1.2 The Free Energy Change on Nucleation

During nucleation only a very small amount of precipitate phase is formed, and the composition of the matrix hardly changes. The most likely nucleus composition will be that which gives the maximum free energy change under these conditions, since this nucleus will have the greatest chance of overcoming the activation barrier to nucleation.

For negligible matrix composition change the free energy change per mole of precipitate is given by the separation of the tangent to the austenite curve, at the bulk composition $\overline{x}$ with

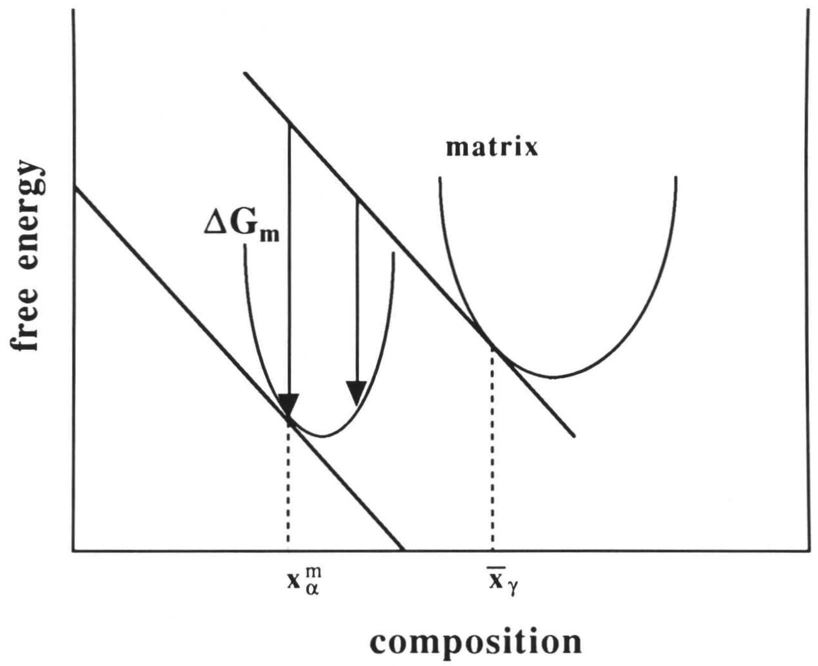

Figure 2.2 Choice of nucleus composition in order to maximise the free energy change on formation of a small amount of precipitate phase. The driving force per mole of nucleus is given by the separation of the ferrite curve from the tangent to the austenite curve at the bulk composition.

the ferrite curve at the composition of the precipitate. The maximum value of the free energy change will be for the ferrite composition x_m where a parallel tangent touches the ferrite curve, as is shown in Figure 2.2. The condition can be described as

$$\left.\frac{\partial G^\alpha}{\partial x}\right|_{x_m} = \left.\frac{\partial G^\gamma}{\partial x}\right|_{\overline{x}} \tag{2.12}$$

This equation can be obtained by differentiating the free energy expressions above, and solving for x_m numerically. The maximum free energy change ΔG_m is then

$$\Delta G_m = RT \ln \left\{ \frac{a_C^\gamma|_{\overline{x}}}{a_C^\alpha|_{x_m}} \right\} \tag{2.13}$$

2.1.3 Thermodynamics of Nucleation of Bainite and Widmanstätten Ferrite

Theory states that nucleation of Widmanstätten ferrite and bainite occurs when ΔG_m is greater than a critical (temperature dependent) value G_N.

$$G_N = 3.636T - 2540 \ \text{J mol}^{-1} \tag{2.14}$$

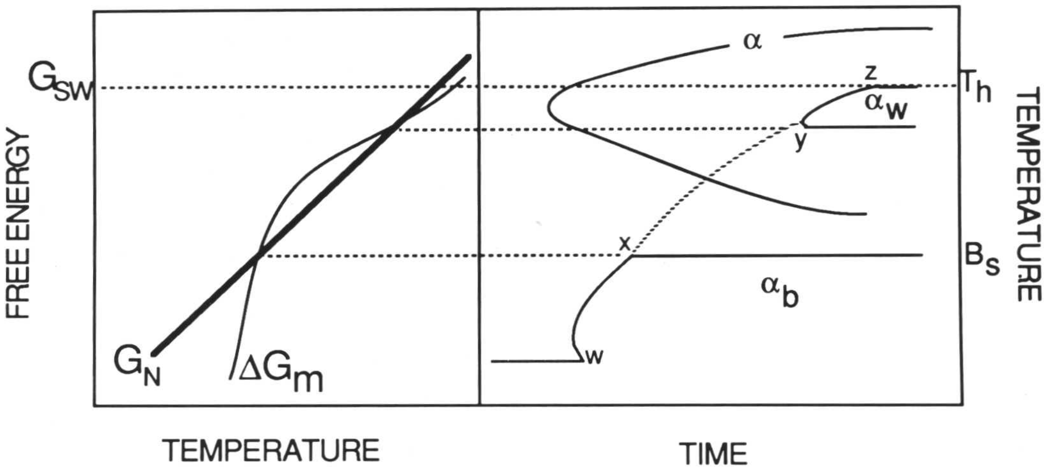

Figure 2.3 Widmanstätten ferrite formation is impossible at intermediate temperatures where the driving force ΔG_m is less than the critical value given by the G_N curve. The lower C-curve then seperates into regions giving Widmanstätten ferrite and bainite.

It has been calculated (Svensson & Bhadeshia, 1988) that in the case of some weld metals the ΔG_m curve intersects with G_N at two temperatures, resulting in a region at intermediate temperature where nucleation is impossible. This case is shown in Figure 2.3. For the cases in which nucleation is possible, in the upper region Widmanstätten ferrite forms, whereas in the lower region nucleation leads to bainite formation.

2.1.4 Thermodynamics of Growth of Bainite

For growth by a diffusionless transformation it is necessary for there to be a negative free energy change for the formation of α of the same composition as the γ matrix. Because of the elastic stored energy of bainite, an additional 400 J mol^{-1} is also required. The locus of temperatures on the phase diagram at which the change from austenite to ferrite of the same composition becomes possible is called the T_0 curve. For strained ferrite, as in bainite, the modified curve is designated T_0'.

The effect of this requirement is to shift the free energy curve of ferrite relative to that of austenite. This is represented in Figure 2.4 which also shows the T_0 and T_0' curves where austenite has the same free energy as unstrained and strained ferrite respectively.

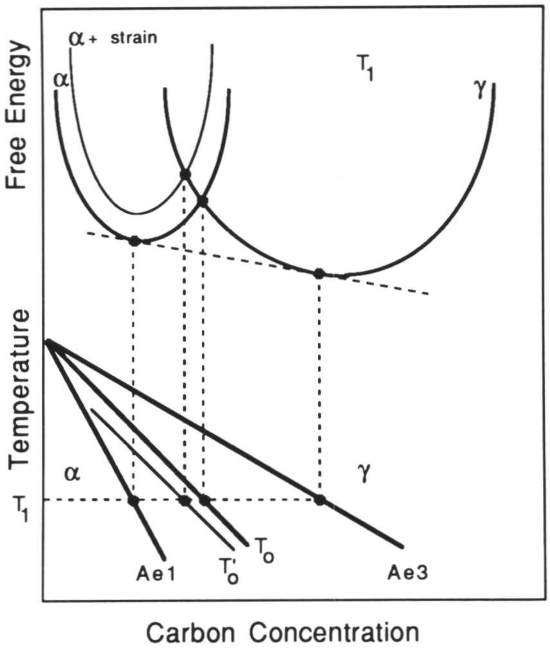

Figure 2.4 Free energy curves for ferrite and austenite, and T_0 curve locus.

As the temperature decreases it first becomes thermodynamically possible to form bainite when the temperature lies below the T_0' curve for the given composition, as long as nucleation is also possible. Also, as isothermal transformation proceeds, when the untransfformed austenite becomes carbon–enriched to such an extent that the T_0' curve is reached, transformation must cease.

2.1.5 Modelling of Martensitic Nucleation

Since bainite is thought to be a product of diffusionless displacive reaction, with excess carbon rejected into the residual austenite subsequent to transformation, it can be considered similar to martensite. The essential difference between the phases results from the fact that martensite nucleates without diffusion of carbon.

The martensitic transformation occurs by the motion of a glissile interface between the ferrite and austenite. The dislocations in such an interface cannot have their Burgers vectors in the interface plane. If this condition is satisfied, the interface can advance without the need for diffusion.

A stacking fault on closest packed planes forms a thin layer of ferrite within the parent austenite. If such a fault has an n planes, each of area A, and the molar density of atoms on the planes is ρ then the total fault energy W is

$$W = n\rho A(\Delta G^{\text{chem}} + E^{\text{str}}) + 2\sigma\{n\} \tag{2.15}$$

where ΔG^{chem} is the molar chemical free energy difference between the two phases, E^{str} is the molar strain energy and σ is the surface energy per unit area of the particle.

By applying the criterion that the barrier to growth is the flow stress of the dislocations in the glissile interface between the matrix and embryo, an expression is formed defining the critical size of particle. If the dislocations require a stress τ_0 for motion, the force per unit length necessary to seperate the dislocations, each of Burgers vector $\mathbf{b}$ is

$$n\tau_0 b \tag{2.16}$$

A fault of energy W will exert a force $-W$ on such an array. The fault will therefore exert sufficient force when

$$n^* \rho A(\Delta G^{\text{chem}} + E^{\text{str}}) + \tau_0 b = -2\sigma \tag{2.17}$$

where n^* is the number of planes in the critical nucleus. If the flow stress of the dislocations has an athermal component as well as a component dependent on temperature, the isothermal and thermal type of martensitic transformations can be rationalised. The activation energy of dislocation motion under an applied stress τ can be represented as

$$Q = Q_0 + (\tau - \tau_\mu)v^* \tag{2.18}$$

where τ_μ is the athermal component of the flow stress and v^* is the activation volume of the nucleus.

If there exists a maximum and minimum rate at which the interface can advance, $\dot{r}_{\text{max}}$ and $\dot{r}_{\text{min}}$ respectively, depending on how the quantities $nb\tau_0$ and W vary with temperature, different steels can fall into the isothermal or athermal transformation regimes. This is shown in Figure 2.5.

As temperature increases the magnitude of the term $-nb\tau_0$ changes until it reaches its athermal value $nb\tau_\mu$. For different materials the variation of W is shown schematically in the figure. If the curves cross at a temperature where the flow stress has its athermal value then martensitic transformation will be athermal since the extent of transformation then depends only on the number of nuclei that have been activated. If transformation becomes possible in the regime where flow stress is temperature dependent the activation energy is dependent on the driving force and isothermal transformation will occur. C-curve type kinetics are also expected, since, as shown in Figure 2.5, there is a temperature at which the chosen value of $\dot{r}$ is at a maximum.

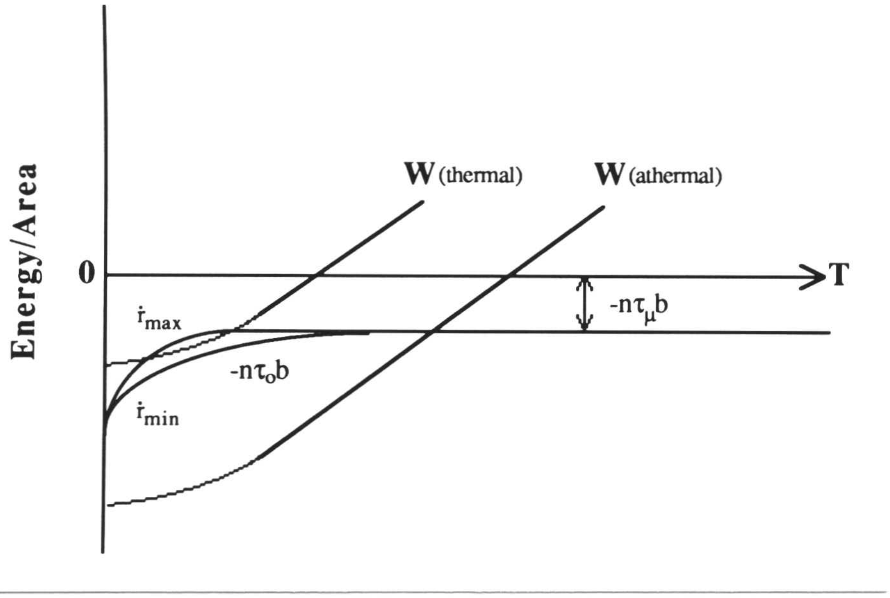

Figure 2.5 Isothermal and athermal martensite nucleation regimes.

Under isothermal transformation conditions the activation energy for nucleation then becomes

$$Q = Q_0 + (\tau_\mu + \frac{\rho A E^{str}}{b} + \frac{2\sigma}{nb})v^* + (\frac{\rho v^*}{b})\Delta G^{\text{chem}} \tag{2.19}$$

2.1.6 TTT Diagram Theory and Application

Extensively used in designing heat treatments for steels, isothermal transformation diagrams, or Time–Temperature–Transformation (TTT) diagrams represent the time necessary for a reaction to initiate at a given temperature. The diagrams are particularly useful in identifying the temperature regions in which different transformation products form. This identification becomes increasingly easy as the substitutional alloying element content of the steel is increased to such an extent that reconstructive and displacive reactions are separated into two distinct regions, each possessing its own characteristic C-curve. The typical effect of increasing alloying elements concentration is shown in Figure 2.6.

In a model for predicting steel microstructure it is of great importance to be able to predict the onset time for a given transformation. For isothermal transformation the incubation time τ corresponds to the time taken for a detectable amount of the precipitate phase to form. For continuous cooling experiments, it it possible to predict the onset time and temperature from knowledge of the TTT diagram, using the Scheil approximation. The cooling curve is first

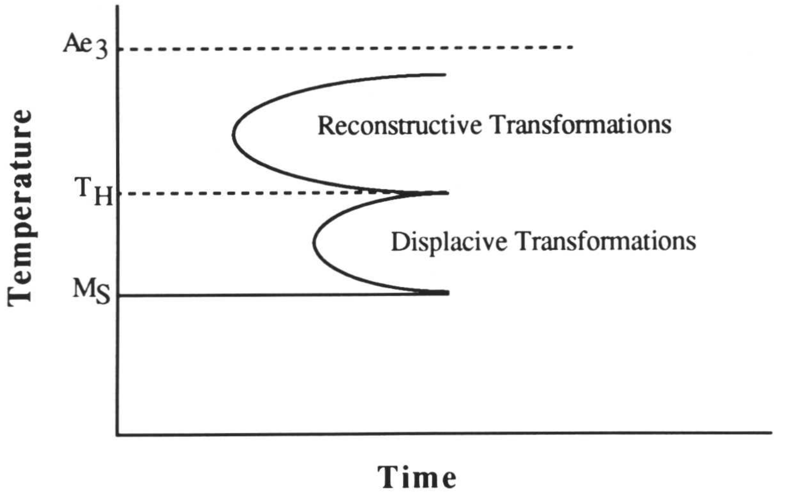

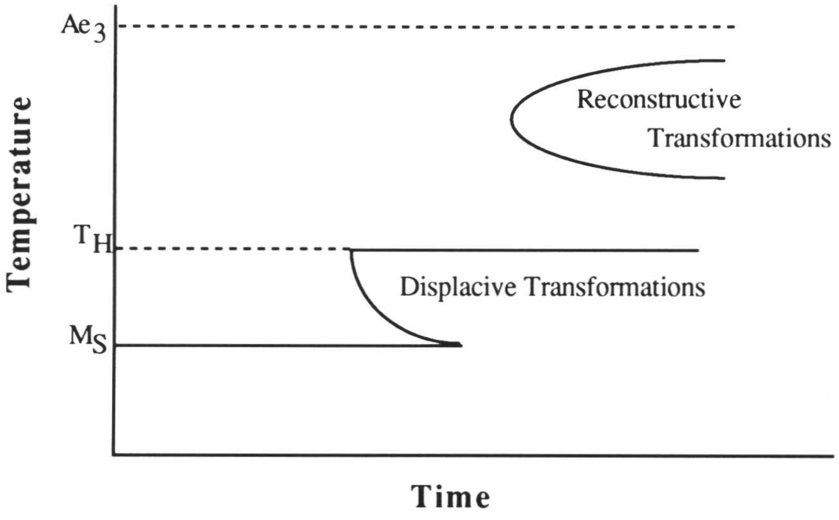

Figure 2.6 The effect on a typical isothermal transformation diagram of increasing the alloying element concentration in the steel. a) low substitutional alloy content b) increased substitutional alloy content.

approximated as a series of isothermal step treatments, the i^{th} step at T_i being of length t_i. Transformation is calculated to begin when the sum

$$\sum_{1}^{i} t_i/\tau_i = 1 \tag{2.20}$$

where τ_i represents the incubation period at T_i. Mathematical modelling of the incubation time period is therefore of great use. A successful model, based on the semi-empirical analysis of existing TTT diagrams was published by Bhadeshia (1982). The incubation time is considered to follow a relationship analogous to that which the steady-state nucleation incubation time follows for reconstructive transformation (Russell 1968, 1969) *i.e.*

$$\tau \propto \frac{T}{(\Delta G_m^v)^p D} \tag{2.21}$$

where ΔG_m^v represents the maximum volume free energy change on nucleation of a small amount of precipitate, D represents the appropriate diffusion coefficient, T the absolute temperature and p a parameter linked to nature of the nucleus.

For prediction of steel TTT diagrams there is insufficient knowledge concerning the nature of the nucleus to allow fundamental choices of p and D, so these parameters were derived merely by curve fitting. D is temperature related in the following way

$$D \propto \exp\{S/R\} \exp\{-Q/RT\} \tag{2.22}$$

where S and Q are the diffusion entropy and enthalpy respectively, which are themselves temperature dependent. The resulting equation used to fit the theory to the experimental values of τ has the form

$$\ln\left\{\frac{\tau\,(\Delta G_m)^p}{T^z}\right\} = \frac{Q'}{RT} + C_4 \tag{2.23}$$

where the term z accounts for the temperature dependence of diffusion enthalpy and entropy. Parameters p and z and C_4 are then optimised in order to produce the maximum correlation with the experimental data.

The results of this semi-empirical analysis are accurate, especially when combined with the other predictable properties of TTT diagrams. The flat top appearance of the lower C–curve when nucleation of displacive transformations first becomes possible, at temperatures below which the thermodynamic growth criterion of bainite has been satisfied, is reproduced by cutting off the lower C–curve at this temperature. The lower curve is also cut off at the M_S temperature which can be predicted thermodynamically (Bhadeshia 1981a, 1981b).

2.1.7 Kinetics of Allotriomorphic Ferrite Formation

Diffusion–controlled growth means that the rate of interface motion is governed by the transport of atoms to and from the interface. In all cases experimental evidence supports the view that allotriomorphic ferrite forms by diffusion–controlled growth.

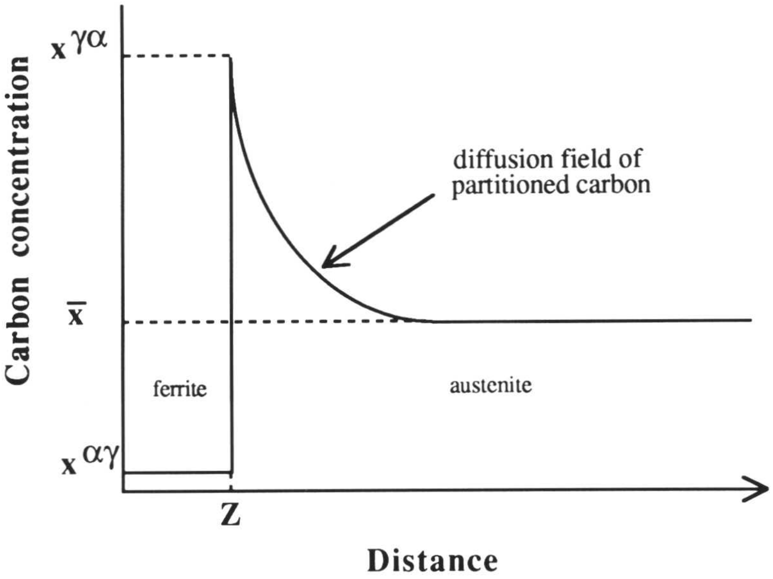

Figure 2.7 Composition profiles for diffusion controlled growth of ferrite in a plain carbon steel.

In plain carbon steels of bulk carbon composition $\overline{x}$, with ferrite and austenite interface compositions $x^{\alpha\gamma}$ and $x^{\gamma\alpha}$ respectively, with an advancing interface of position Z, the composition profile in the austenite is shown in Figure 2.7. From dimensional arguments (Christian 1975) it is argued that the interface position for diffusional growth has the form

$$Z = \alpha_1 t^{1/2} \tag{2.24}$$

where Z is the position of the interface on the z axis. The constant of proportionality α_1 is known as the parabolic thickening constant.

At the ferrite/austenite interface Fick's law states that

$$\frac{\partial x_1}{\partial t} = \frac{\partial}{\partial z}\left(D_{11}\left\{x_1\right\}\frac{\partial x_1}{\partial z}\right) \tag{2.25}$$

where x_1 refers to the mole fraction of carbon, D_{11} is the diffusion coefficient of carbon in austenite. Mass balance considerations give the following relationship

$$dZ\left(x^{\gamma\alpha} - x^{\alpha\gamma}\right) = D_{11}\left|\frac{\partial x_1}{\partial z}\right|_{z=Z} dt \tag{2.26}$$

where $x^{\alpha\gamma}$ and $x^{\gamma\alpha}$ are the interface compositions of ferrite and austenite respectively. The parabolic rate constant to be related to the interface conditions by the equation

$$\frac{\alpha_1 t^{-1/2}}{2}\left(x^{\gamma\alpha} - x^{\alpha\gamma}\right) = D_{11}\left|\frac{\partial x_1}{\partial z}\right|_{z=Z} \tag{2.27}$$

In general the diffusion coefficient is concentration dependent and so assumptions about the form of the variation have to be made. A useful approximation is to substitute the weighted average diffusivity $\underline{D_{11}}$ for the diffusion coefficient of carbon. This enables analytical solutions to the differential equations to be obtained.

$$\underline{D_{11}} = \int_{\overline{x}}^{x^{\gamma\alpha}} \frac{D_{11}\{x'\}\,dx'}{(x^{\gamma\alpha} - \overline{x})} \tag{2.28}$$

Alloy Steels: Local Equilibrium Growth

In Fe–X–C alloys, X being a substitutional alloying element, an added complication of diffusion of the substitutional alloying element arises. In general, the diffusivities of the interstitial and substitutional species are vastly different. For equilibrium to be maintained at the interface, and for the transport requirements of all atoms from the interface to be satisfied simultaneously *i.e.* the interface velocity V_{int} must satisfy the simultaneous equations

$$\left(x_1^{\gamma\alpha} - x_1^{\alpha\gamma}\right) V_{\text{int}} = D_{11}\nabla x_1 \tag{2.29}$$

and

$$\left(x_2^{\gamma\alpha} - x_2^{\alpha\gamma}\right) V_{\text{int}} = D_{22}\nabla x_2 \tag{2.30}$$

where x_1 and x_2 are the concentrations of carbon and X respectively, with D_{22} being the diffusion coefficient of the substitutional solute. The superscripts $\alpha\gamma$ and $\gamma\alpha$ denote the *interface* values of x_1 and x_2 in the ferrite and the austenite respectively.

Because $D_{11} \gg D_{22}$ the bulk alloy equilibrium compositions cannot be adopted by the interface whilst simultaneously satisfying the flux equations for carbon and X. Modified values are adopted instead, bringing the transport of both species to the required level whilst maintaining local equilibrium at the boundary. For such conditions the growth still follows parabolic interface advancement.

$$Z = \alpha_1 t^{1/2} = \eta_1\left(D_{11}t\right)^{1/2} = \eta_2\left(D_{22}t\right)^{1/2} \tag{2.31}$$

where η_1 and η_2 are growth constants. The interface compositions can be calculated since only one of $x^{\alpha\gamma}$, $x_2^{\alpha\gamma}$, $x^{\gamma\alpha}$, $x_2^{\gamma\alpha}$ are independent (Coates 1973).

Alloy Steels: Paraequilibrium Growth

In a ternary alloy, if the mole fractions of carbon, a substitutional alloying element and iron are x, x_2 and x_3 respectively, under paraequilibrium conditions the ratio

$$\frac{x_2}{x_3}$$

is constant across the α/γ boundary during ferrite growth. Carbon adopts paraequilibrium interface compositions giving it equal chemical potential in both phases across the interface.

The transition from local to paraequilibrium is thought to occur at interface velocities of the kind that would involve the concentration spike associated with the substitutional alloy element during NPLE growth becoming small with respect to interatomic distances, in which case its physical significance is gone. It has been suggested that, if z_{2d} represent the extent of the diffusion field of the substitutional alloy element the the transition from local to paraequilibrium occurs when (Coates, 1973)

$$z_{2d} = \frac{2D_{22}}{V_{\text{int}}} \tag{2.32}$$

2.2 Bainite Overall Transformation Kinetics Model

This model was proposed by Bhadeshia (1982b) in order to incorporate the then recently–developed theories on the displacive nucleation and growth of bainite into a self–consistent model. Since modifications are made in this work, in order to correct certain errors in the original model, it is necessary to present the original theory in detail.

Thermodynamically it is impossible to form bainite if the carbon concentration of the austenite is greater than or equal to the $x_{T_0'}$ composition (Bhadeshia & Edmonds, 1980). Therefore, at a given temperature below B_S there exists a maximum possible ferrite volume fraction θ, where

$$\theta = \frac{x_{T_0'} - \overline{x}}{x_{T_0'} - x^{\alpha}} \tag{2.33}$$

where $x_{T_0'}$ and therefore θ are functions of temperature. It is then convenient to define a normalised volume fraction ξ

$$\xi = v/\theta \tag{2.34}$$

where v is the actual ferrite volume fraction, θ being the limiting volume fraction.

For consistency with martensite nucleation theory, nucleation of bainite is considered to have an activation energy proportional to the nucleation driving force ΔG_m. *i.e.*

$$I = C_1 \exp\left\{\left(\frac{C_2 - C_3 \Delta G_m}{RT}\right)\right\} \tag{2.35}$$

where C_1, C_2 and C_3 are constants. At the W_S temperature, when ΔG_m equals G_N (Bhadeshia 1981a)

$$I = I_{W_S} \exp\left\{-\frac{C_2 \Delta T}{RTW_S} - \frac{C_3}{R}\left(\frac{\Delta G_m}{T} - \frac{G_N}{W_S}\right)\right\} \tag{2.36}$$

ΔG_m will vary as the reaction proceeds because the carbon partitioned from the bainitic ferrite will enrich the untransformed austenite. The effect of such enrichment on ΔG_m is modelled as a linear function of the extent of reaction in the following way

$$\Delta G_m = \Delta G_m^0 (1 - (C_4/C_3)\theta\xi) \tag{2.37}$$

with C_4 being a constant, hence

$$I = I_{W_S} \exp\left\{-\frac{C_2 \Delta T}{RTW_S} - \frac{C_3}{R}\left(\frac{\Delta G_m^0}{T} - \frac{G_N}{W_S}\right)\right\} \exp\left\{\frac{\Delta G_m^0 C_4 \theta\xi}{RT}\right\} \tag{2.38}$$

Bainite is known to exhibit autocatalysis, where the presence of previously formed ferrite increases the nucleation rate of further plates (Bhadeshia & Christian, 1990). This can be approximated as a linear increase in nucleation site density with true volume fraction *i.e.*

$$I_{W_S} = I_0 (+\beta\theta\xi) \tag{2.39}$$

where β is the auto-catalysis constant. Representing

$$\Gamma = \frac{\Delta G_m^{\ 0} C_4 \theta}{RT} \tag{2.40}$$

this gives

$$I = I_0 \exp\left\{-\frac{C_2 \Delta T}{RTW_S} - \frac{C_3}{R}\left(\frac{\Delta G_m^{\ 0}}{T} - \frac{G_N}{W_S}\right)\right\} \exp\{\Gamma\xi\} \tag{2.41}$$

Forming a differential equation according to the theories of Johnson, Mehl & Avrami, modified for the case of transformation to a limiting volume fraction (Christian 1975).

$$\frac{\theta d\xi}{dt} = uI\{\xi\}(1-\xi) \tag{2.42}$$

where u is the average volume of a bainitic sub–unit. The equation can be separated into partial fractions

$$\int_0^\xi \frac{A d\xi}{(1-\xi)} + \int_0^\xi \frac{B d\xi}{(1+\beta\theta\xi)} + \int_0^\xi C \exp\{-\Gamma\xi\} d\xi$$

$$= \frac{uI_0}{\theta} \exp\left\{-\frac{C_2 \Delta T}{RTW_S} - \frac{C_3}{R}\left(\frac{\Delta G_m^{\ 0}}{T} - \frac{G_N}{W_S}\right)\right\} t \tag{2.43}$$

where A, B and C are the constants arising from the separation of the equation into partial fractions.

$$A = \frac{\exp\{\Gamma\}}{(1+\beta\theta)} \tag{2.44}$$

$$C = \frac{1 - e^{\Gamma/\beta}(1 - 1/\beta + A/\beta + A\theta)}{(1 - 1/\beta)\left(1 + \theta - e^{\Gamma/\beta}\right)} \tag{2.45}$$

$$B = 1 - C - A \tag{2.46}$$

The equation can be solved analytically giving the solution

$$t = \frac{\theta\left(-A\ln\{1-\xi\} + (B/\beta\theta)\ln\{1+\beta\theta\xi\} + (C/\Gamma)\left(1 - e^{-\Gamma\xi}\right)\right)}{uI_0 \exp\left\{-\frac{C_2 \Delta T}{RTW_S} - \frac{C_3}{R}\left(\frac{\Delta G_m^{\ 0}}{T} - \frac{G_N}{W_S}\right)\right\}} \tag{2.47}$$

where t represents the time taken to reached a normalised volume fraction ξ at a temperature T.

By optimisation of the fit between the theory and data from dilatometric transformation and three high–silicon steels the constants were evaluated as

$$\beta = 200 \tag{2.48}$$

$$uI_0 = 1.234 \times 10^{-4} \text{s}^{-1} \tag{2.49}$$

$$C_2 = 29710 \text{ J mol}^{-1} \tag{2.50}$$

$$C_3 = 3.769 \tag{2.51}$$

$$C_4 = 11 \tag{2.52}$$

This model was shown to give better agreement between predicted and experimental values of the reaction time t than conventional Avrami–type expressions for steels containing sufficient silicon to prevent other reactions, such as carbide precipitation, from interfering with the bainite transformation (Bhadeshia 1982b). The model, however, makes no attempt to model the growth of the ferrite plates, transformation is assumed to occur by the repeated nucleation of plates which appear from the matrix fully formed.

CHAPTER 3

A Modified Bainite Transformation Kinetics Model

3.1 Introduction

The earlier model for the overall transformation kinetics of bainite is corrected and modified here to be consistent with known details of the mechanisms of bainitic nucleation and growth. A comparison with published experimental data shows that the model is capable of accurately representing the development of transformation as a function of alloy chemistry and temperature.

There is currently a large increase in the demand for bainitic steels, cast irons and weld deposits for a wide variety of applications ranging from rail steels to accelerated cooled low-carbon steels for structural engineering (Bhadeshia, 1989; Edmonds & Cochrane, 1990). The research effort backing these developments could benefit greatly from kinetic theory capable of predicting the bainitic microstructures as a function of alloy chemistry and thermomechanical treatment.

The problem is complicated by the fact that there are several microstructural scales to consider (Figure 3.1). The transformation usually begins at the austenite grain surfaces with the nucleation and growth of individual platelets of ferrite. The displacements that occur during growth represent a shape change which is an invariant-plane strain (IPS) with a large shear component (Ko & Cottrell, 1952). The growth of the platelet is stifled by the dislocation debris created as the IPS shape change is plastically accommodated (Bhadeshia & Edmonds, 1979, 1980). The platelets thus grow to a limited size which is usually smaller than the austenite grain size. Further transformation occurs by the formation of new, parallel platelets in clusters known as sheaves; the platelets are therefore called the *sub-units* of the sheaf (Heheman, 1970).

It is believed that the sub-units grow without diffusion, but that any excess carbon in the ferrite is soon afterwards partitioned into the residual austenite (Christian & Edmonds, 1984; Bhadeshia & Christian, 1990). The indications are that the time required to grow a sub-unit is small relative to that needed to nucleate successive sub-units (Bhadeshia, 1984; Ali & Bhadeshia, 1989). The growth rate of individual sub-units (Bhadeshia, 1984) is known to be much faster than the lengthening rate for sheaves (Bhadeshia & Christian, 1990; Ali & Bhadeshia, 1989; Goodenow, Matas & Hehemann, 1963; Speich & Cohen, 1960; Rao & Winchell, 1967).

The overall transformation kinetics include the simultaneous growth and impingement of many different sheaves. A further complication is that carbide precipitation may eventually occur from the carbon-enriched residual austenite, or in the case of lower bainite, from the

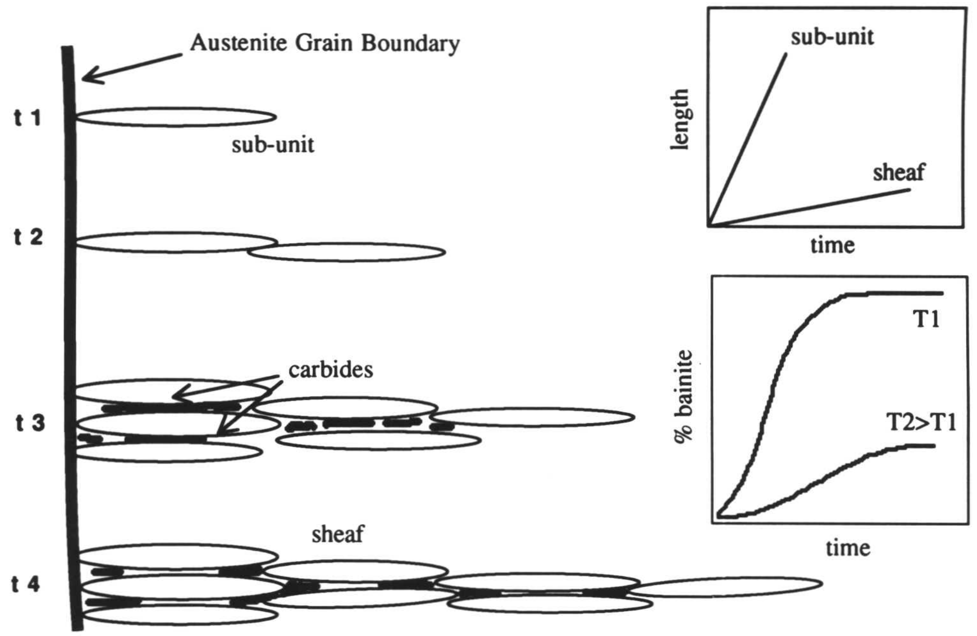

Figure 3.1 Schematic illustration of the variety of stages in the development of a bainitic microstructure.

supersaturated ferrite. Carbide precipitation is not addressed in this study, which is confined to situations where the use of alloying additions such as silicon prevent such precipitation. Fortunately, it turns out that the vast majority of bainitic steels which are being actively considered for major applications do not involve carbide precipitation.

The purpose of the work presented here was to develop a model for the overall transformation kinetics, based on the mechanism of the bainite transformation. Such a model was last attempted by Bhadeshia (1982b), but as will be seen in the next section, it contains a number of important discrepancies.

3.2 Problems with the Earlier Theory

In steels containing a relatively large concentration of silicon (> 1.5 wt.%), the precipitation of carbides can be suppressed, especially when the transformation temperature is in the upper bainite range. We have noted that bainitic ferrite sub–units grow without diffusion, but that any excess carbon is soon afterwards partitioned into the residual austenite. This makes it more difficult for subsequent sub–units to grow as the austenite becomes stabilised by its increased carbon concentration. The maximum extent to which the bainite reaction can proceed is therefore determined by the composition of the residual austenite. Bainite growth must cease when the free energies of austenite and ferrite of identical composition become equal. The locus of all points on a temperature/carbon concentration plot, where austenite and ferrite of identical chemistry have equal free energies, is called the T_0 curve; when this is modified to allow for bainite's stored energy of some 400 J mol^{-1} (Bhadeshia & Edmonds 1980; Bhadeshia & Christian, 1990), the locus becomes the T_0' curve. Thus, the diffusionless growth of bainitic ferrite becomes impossible when the carbon concentration of the residual austenite reaches the T_0' concentration. This maximum volume fraction is termed θ. The normalised volume fraction ξ is then defined as

$$\xi = v/\theta \tag{3.1}$$

where v is the actual volume fraction of bainitic ferrite.

The activation energy for the nucleation of bainite is known to be directly proportional to the driving force for transformation (Magee, 1970). This is consistent with the theory for martensite nucleation (Magee, 1970; Olson & Cohen 1976), although it is a requirement that carbon must partition into the austenite during bainite nucleation (Bhadeshia, 1981a). The nucleation mechanism of Widmanstätten ferrite and bainite is considered to be identical; a potential nucleus can develop into either phase depending on whether or not an adequate driving force is available for the growth of bainite at the transformation temperature concerned. On this basis, it is possible to define a universal nucleation function of temperature, G_N, which is applicable to all steels. In a given steel, nucleation first becomes possible at a detectable rate below a temperature W_S (the Widmanstätten ferrite–start temperature), at which magnitude of the maximum nucleation free energy change ΔG_m for the steel exceeds that given by G_N (Bhadeshia, 1981a, 1982a; Ali & Bhadeshia, 1990).

According to the original overall transformation kinetics theory developed by Bhadeshia (1982b), the nucleation rate of ferrite per unit volume I, at any temperature T, can be expressed as a multiple of the nucleation rate at the W_S temperature, I_{W_S}:

$$I = I_{W_S} \exp\left\{ -\frac{C_2 \Delta T}{R T W_S} - \frac{C_3}{R}\left(\frac{\Delta G_m}{T} - \frac{G_N}{W_S}\right)\right\} \tag{3.2}$$

where ΔG_m represents the maximum possible free energy change on nucleation, and G_N is the value of the universal curve representing the minimum necessary free energy change for displacive nucleation of ferrite, at the W_S temperature. C_2 and C_3 are empirical constants. ΔG_m is a function of the volume fraction of ferrite, since carbon enrichment of the untransformed austenite will lower the magnitude of the free energy change as the volume fraction of ferrite increases. This effect is modelled as

$$\Delta G_m = \Delta G_m^0 \left(1 - C_4 \theta \xi / C_3\right) \tag{3.3}$$

where ΔG_m^0 is the initial value of ΔG_m, and C_4 is an empirical constant.

The effect of autocatalysis *i.e.* the increase in number density of nucleation sites as the volume fraction of ferrite increases is modelled as

$$I_{W_S} = I_0\,(1 + \beta\theta\xi) \tag{3.4}$$

where β is the empirical autocatalysis constant.

At the onset of transformation, the increment dv of volume fraction of ferrite that forms between times t and $t + dt$ is given by

$$dv = \theta d\xi = Iudt \tag{3.5}$$

where u is the volume of a bainitic sub–unit and I is the nucleation rate per unit volume.

At later stages in the transformation, since the volume of austenite available for transformation will have decreased, it is necessary to consider the increment in the 'extended volume' dv_e (Christian, 1975), which accounts for the formation of 'phantom' nuclei within regions of ferrite already transformed. This enables the use of the nucleation rate of bainite per unit volume of austenite, despite the fact that the volume of austenite is changing, provided that the extended volume increment is related to the real volume increment. This is done in the following way

$$dv = (1 - \xi)dv_e \tag{3.6}$$

where

$$dv_e = Iudt \tag{3.7}$$

which gives

$$\theta d\xi = (1 - \xi)Iudt \tag{3.8}$$

On substituting the expressions for the nucleation rate of bainite this gives

$$\theta\frac{d\xi}{dt} = uI_0(1 - \xi)(1 + \beta\theta\xi)\exp\{\Gamma\xi\}\exp\left\{-\frac{C_2\Delta T}{RTW_S} - \frac{C_3}{R}\left(\frac{\Delta G_m^0}{T} - \frac{G_N}{W_S}\right)\right\} \tag{3.9}$$

where u is the average volume of a single sub–unit, and

$$\Gamma = \frac{C_4\Delta G_m^0}{RT} \tag{3.10}$$

By separating the variables the equation can be integrated

$$\int_0^\xi \frac{Ad\xi}{(1 - \xi)} + \int_0^\xi \frac{Bd\xi}{(1 + \beta\theta\xi)} + C\int_0^\xi \exp\{-\Gamma\xi\}\,d\xi$$

$$= \frac{uI_0}{\theta}\exp\left\{-\frac{C_2\Delta T}{RTW_S} - \frac{C_3}{R}\left(\frac{\Delta G_m^0}{T} - \frac{G_N}{W_S}\right)\right\}\int_0^t dt \tag{3.11}$$

where A, B and C are constants arising from the separation of the differential equation into partial fractions. ΔT is defined as $T - W_S$.

An analytical solution (not presented in the original model) is obtained giving the time t taken to form a normalised volume fraction ξ at the reaction temperature T.

$$t = \frac{\theta\left(-A\ln\{1-\xi\} + (B/\beta\theta)\ln\{1+\beta\theta\xi\} + (C/\Gamma)\left(1-e^{-\Gamma\xi}\right)\right)}{uI_0\exp\left\{-\frac{C_2\Delta T}{RTW_S} - \frac{C_3}{R}\left(\frac{\Delta G_m^0}{T} - \frac{G_N}{W_S}\right)\right\}} \tag{3.12}$$

After optimisation of the model, the best fit values of the empirical constants were found to be (Bhadeshia, 1982b)

$$uI_0 = 1.234 \times 10^{-4} s^{-1} \quad C_2 = 27910 \text{ J mol}^{-1} \quad C_3 = 3.679$$

$$C_4 = 11 \qquad \beta = 200$$

The present studies began with the use of this model as a means to the prediction of weld metal microstructures, but it was soon realised that there are certain important errors.

3.2.1 Prediction Errors

A thorough assessment of the model was made, using thermodynamic parameters and theory (necessary to calculate ΔG_m, for example) described when the model was first proposed (Bhadeshia, 1982b). As is shown in Figure 3.2 the original model incorrectly predicts that, at the same transformation temperature, a steel with a high manganese content will transform at a *faster* rate than a more lightly alloyed steel. This prediction is contrary to experience. Table 3.1 gives the compositions of the steels used for the comparison calculation, which was performed for a reaction temperature of 470°C. This temperature was calculated to lie between the bainite–start and martensite–start temperatures for both alloys. The compositions were chosen to be consistent with the welding alloys that are currently being investigated. The values of ΔG_m^0 and G_N and W_S together with the predicted B_S and M_S were calculated using theory outlined by Bhadeshia (1981a).

The model also predicted for all steels that there was a deceleration in transformation rate as the undercooling below W_S increased. An example is given in Figure 3.3 which shows the calculated transformation curves for the isothermal formation of bainite in 300 M steel (composition given in Table 3.2) at a variety of temperatures within the bainite transformation range. The initial reaction rate is predicted to decrease as the isothermal transformation temperature decreases. This is in spite of the fact that driving force increases as temperature decreases. The calculations also contradict experimental data for 300 M, discussed later in this chapter, which show the opposite trend.

Alloy	C	Si	Mn	Ni	Mo	Cr	B_S/°C	M_S/°C
Steel 1	0.06	0.5	2.0	2.0	0.4	0.6	478	406
Steel 2	0.06	0.5	1.0	2.0	0.4	0.6	565	455

Table 3.1 Steel compositions (wt %) and calculated M_S and B_S temperatures used for comparison of predicted reaction rates.

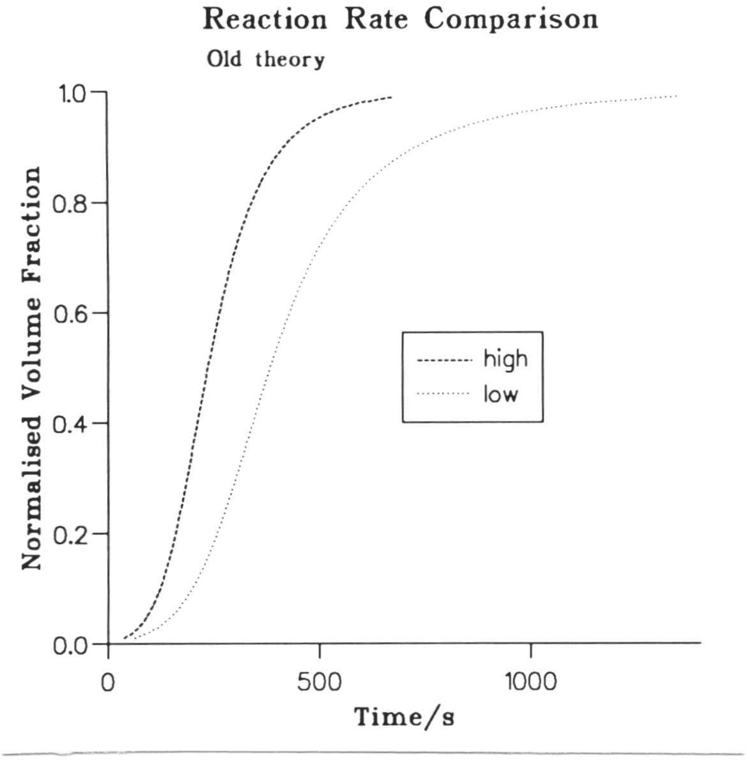

Figure 3.2 The relative reaction rates of a high manganese and a low manganese steel, as predicted by the original bainite transformation kinetics model (Bhadeshia, 1982b). The steel compositions are given in Table 3.1.

3.2.2 Theoretical problems

A key assumption used in the derivation of the universal nucleation function G_N was that at the highest temperature at which ferrite can nucleate by a displacive mechanism (*i.e.* W_S), all steels should have an identical nucleation rate (Bhadeshia, 1981a). The original bainite kinetics model (Bhadeshia, 1982b) is not, in general, consistent with this assumption. This can be shown by comparing the nucleation rates of two steels, A and B, at their W_S temperatures, W_{SA} and W_{SB} respectively. The G_N function represents the minimum driving force necessary to initiate nucleation of ferrite by a displacive mechanism. It is found to be a linear function of temperature (Bhadeshia, 1981a). At the W_S temperature, ΔG_N is given by

$$G_N = pW_S - r \qquad (3.13)$$

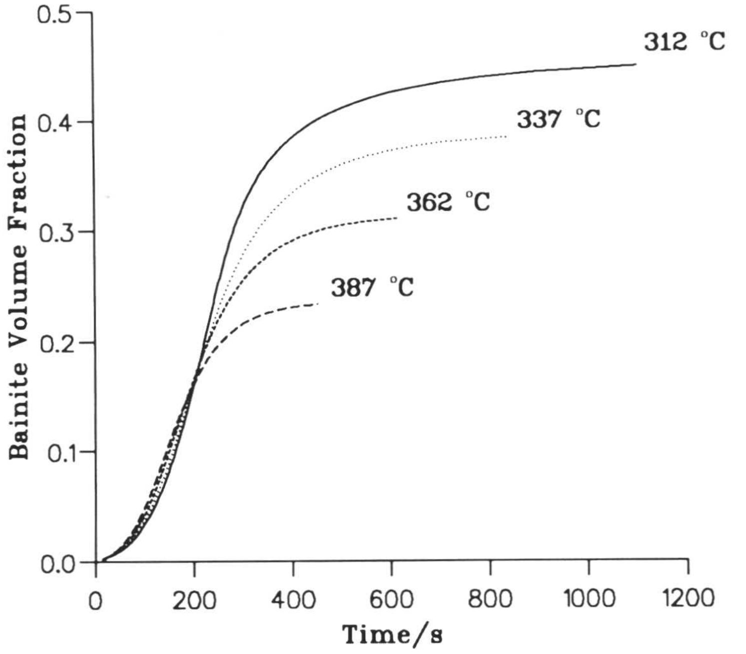

Figure 3.3 Predicted isothermal transformation curves for 300 M steel (Fe–0.44C–1.74Si–0.67Mn–1.85Ni–0.83Mo–0.39Cr–0.09V) calculated using the original bainite transformation kinetics model (Bhadeshia, 1982b). The curves show that the initial reaction rate is predicted to decrease as the temperature decreases.

where p and r are both positive constants. If G_{NA} and G_{NB} represent the values of G_N at W_{SA} and W_{SB} respectively then

$$G_{NA} = pW_{SA} - r \tag{3.14}$$

and

$$G_{NB} = pW_{SB} - r \tag{3.15}$$

where (Ali & Bhadeshia, 1990)

$$p = 3.6375 \qquad r = 2540 \text{ J mol}^{-1}$$

It follows from equation 3.2, that the ratio of nucleation rates in the two steels at their respective W_S temperatures is given by:

$$\frac{I_A}{I_B} = \exp\left\{-\frac{(C_2 - C_3 r)(W_{SB} - W_{SA})}{RW_{SA}W_{SB}}\right\} \tag{3.16}$$

From this equation it can be seen that unless

$$C_2 = C_3 r \tag{3.17}$$

different steels will not have the same nucleation rate at their W_S temperature. The values of the terms derived for the original theory (Bhadeshia, 1982b) are

$$C_2 = 27910 \text{ J mol}^{-1} \quad C_3 = 3.679 \quad r = 2540 \text{ J mol}^{-1}$$

which clearly do not satisfy this condition.

A further difficulty was also identified in the modelling of the effect of carbon enrichment of untransformed austenite on the $\gamma \rightarrow \alpha$ free energy change *i.e.*

$$\Delta G_m = \Delta G_m^0 (1 - C_4 \theta \xi / C_3) \tag{3.18}$$

with the value of C_4/C_3 equal to 2.98. This equation predicts that the value of ΔG_m will be positive after a volume fraction of bainite of 0.34 has formed, regardless of temperature or alloy chemistry.

Bainite is observed to grow until the carbon content of the untransformed austenite reaches the value given by the T_0' for the steel. The limiting volume fraction of bainite is therefore a function of temperature and alloy chemistry. It is not therefore reasonable for transformation to cease when a volume fraction of 0.34 is achieved. Indeed, the isothermal transformation data used for the investigation of the original model shows many cases where the volume fractions far greater than 0.34. This can be seen in Figures 3.5–3.7, which show the data for the steels Fe–Mn–Si–C, Fe–Ni–Si–C and 300 M respectively (Bhadeshia, 1982b).

3.3 Development of a New Model

3.3.1 The Nucleation Rate at W_S

To ensure that the activation energy for nucleation remains directly proportional to ΔG_m (Bhadeshia, 1982b), and imposing the condition that the nucleation rate at W_S is constant for all steels, the expression for the nucleation rate of bainite is modified to become

$$I = K_1 \exp\left\{ -\frac{K_2}{RT} - \frac{K_2 \Delta G_m}{rRT} \right\} \tag{3.19}$$

where K_1 and K_2 are constants, denoted by the letter K in order to avoid confusion with the constants of the original theory. K_1 represents the number density of potential sites for nucleation. At W_S the expression becomes

$$I = K_1 \tag{3.20}$$

regardless of the alloy composition.

3.3.2 The Effect of Carbon Partitioning on Free Energy Change

As transformation proceeds it becomes necessary to account for the decrease in driving force due to the carbon-enrichment of untransformed austenite. The effect of auto-catalysis also becomes important.

As mentioned above, the formation of bainite can only occur when the thermodynamic criteria for both nucleation and growth are satisfied. At the onset of transformation the criterion for nucleation is that

$$\Delta G_m < G_N \tag{3.21}$$

and the growth criterion is that the driving force for transformation without a composition change exceeds the stored energy of bainite:

$$\Delta G^{\gamma \rightarrow \alpha} < -400 \text{ J mol}^{-1} \tag{3.22}$$

This last expression defines the T_0' curve, but both the nucleation and growth criteria must be satisfied during transformation. As the austenite carbon concentration increases during transformation, the magnitude of both ΔG_m and $\Delta G^{\gamma \rightarrow \alpha}$ will decrease. Eventually the reaction will cease when one criterion is not satisfied. The value of θ, the maximum allowable volume fraction at the reaction temperature, is taken as the ferrite volume fraction when reaction ceases, regardless of whether termination is by a failure of the nucleation or the growth criterion.

Let x_{N_0} represents the austenite carbon concentration when the nucleation criterion fails and $x_{T_0'}$ when the growth criterion fails. If the driving force is assumed to vary linearly with the extent of reaction, between its initial value ΔG_m^0 and its final value when the reaction terminates, then

$$\Delta G_m = \Delta G_m^0 - \xi(\Delta G_m^0 - G_N) \tag{3.23}$$

This equation is inaccurate when $x_{N_0} > x_{T_0'}$, but this is not a significant problem since the model also includes a growth criterion in which reaction ceases when the fraction θ is achieved. The form of the equation has the additional advantage in that the linear function of ξ preserves the ability to integrate the final differential equation representing the overall transformation kinetics analytically.

A comparison of the x_{N_0} and $x_{T_0'}$ curves for the steel 300 M is shown in Figure 3.4, demonstrating that they are in fact quite close to each other, and that both curves lie well below the Ae_3' curve which is the $\alpha + \gamma/\gamma$ paraequilibrium phase boundary.

3.3.3 Autocatalysis

Steels with a high carbon concentration eject more carbon from the newly transformed ferrite than lower carbon steels. The build up of carbon at the ferrite–austenite interfaces

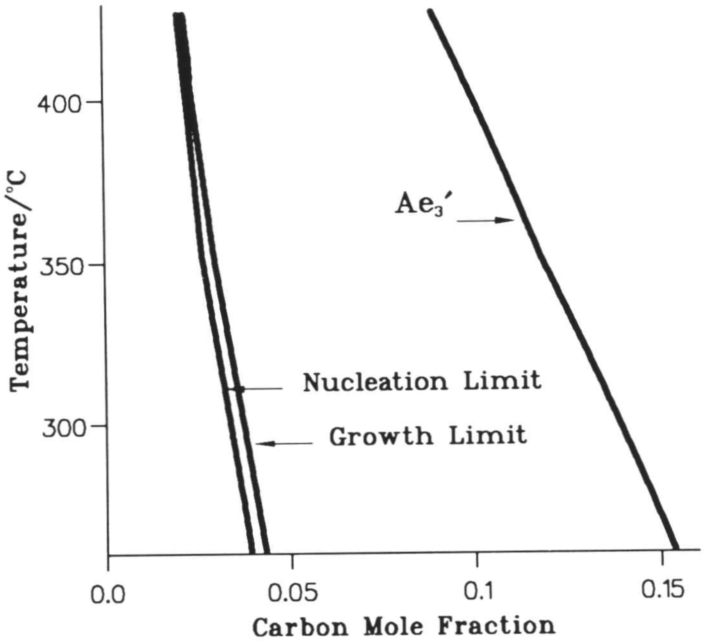

Figure 3.4 Comparison of the x_{N_0} and $x_{T_0'}$ curves for the steel 300 M. The $Ae3'$ curve represents the paraequilibrium $\alpha + \gamma/\gamma$ phase boundary.

will cause a temporary local decrease in the driving force for diffusionless transformation. The process of further nucleation on the previously formed plates (*i.e.* autocatalysis) will be inhibited by this carbon build up. This suggests that the autocatalysis factor used in the kinetics model should in some way be dependent on the overall carbon concentration of the alloy. For simplicity the following assumption is used

$$\beta = \lambda_1 (1 - \lambda_2 \overline{x}) \tag{3.24}$$

where $\overline{x}$ represents the mean carbon concentration of the alloy, and β is the autocatalysis factor (equation 3.4) with λ_1 and λ_2 being empirical constants. In this way, the effect of autocatalysis is less for high carbon steels than for those with lower carbon content. The additional nucleation sites introduced as transformation proceeds is then specified by equation 3.4.

3.3.4 The Effect of Austenite Grain Size

The original model neglected to include a specific austenite grain size effect. The nucleation rate of a grain boundary–nucleated transformation can be assumed to be proportional to the surface area of austenite grain boundaries per unit volume S_V. The reason for this is that the number of suitable sites for nucleation is expected to be directly proportional to the surface area of γ/γ grain boundaries within the sample.

Stereological theory relates S_V to the mean linear intercept $\overline{L}$ of a series of random lines with the austenite grain boundaries, by the expression (DeHoff & Rhines, 1968)

$$S_V = 2/\overline{L}. \tag{3.25}$$

In the new expression for the nucleation rate of bainite the term K_1 will be a function of the austenite grain size, as expressed by the mean linear intercept

$$K_1 = (\overline{L}K_1')^{-1} \tag{3.26}$$

where K_1' is an empirical constant.

3.3.5 Final Expression

The modifications discussed above can be incorporated into a new model as follows. The volume fraction increment between times t and $t + dt$ is

$$\theta d\xi = (1 - \xi)uI dt \tag{3.27}$$

where u is the sub–unit volume and I is the nucleation rate of bainite per unit volume. The expression for the nucleation rate of bainite can be substituted into this equation giving a differential equation for the overall transformation rate of bainite

$$\frac{d\xi}{dt} = \frac{uK_1}{\theta}(1 - \xi)(1 + \beta\theta\xi)\exp\left\{-\frac{K_2}{RT}\left(1 + \frac{\Delta G_m^{\,0}}{r}\right) + \Gamma_2\xi\right\} \tag{3.28}$$

where Γ_2 is given by

$$\Gamma_2 = \frac{K_2(\Delta G_m^{\,0} - G_N)}{rRT} \tag{3.29}$$

The solution of this equation has the same form as in the previous theory *i.e.*

$$t = \frac{\theta\left(-A\ln\{1 - \xi\} + \frac{B}{\beta\theta}\ln\{1 + \beta\theta\xi\} + \frac{C}{\Gamma_2}\left(1 - e^{-\Gamma_2\xi}\right)\right)}{uK_1\exp\left\{-\frac{K_2}{RT} - \frac{K_2\Delta G_m^{\,0}}{rRT}\right\}} \tag{3.30}$$

The constants were determined by optimising the theory using the same data as used by Bhadeshia (1982b). In this way a direct comparison between the two theories can be obtained.

3.3.6 Interpretation of the Experimental Data

The compositions of the steels used for the original analysis are given in Table 3.2.

	C	Si	Mn	Ni	Mo	Cr	V
Fe–Mn–Si–C	0.22	2.03	3.00	0.00	0.00	0.00	0.00
Fe–Ni–Si–C	0.39	2.05	0.00	4.08	0.00	0.00	0.00
300 M	0.44	1.74	0.67	1.85	0.83	0.39	0.09

Table 3.2 Compositions (wt.%) of the steels used for determination of the reaction kinetics of bainite.

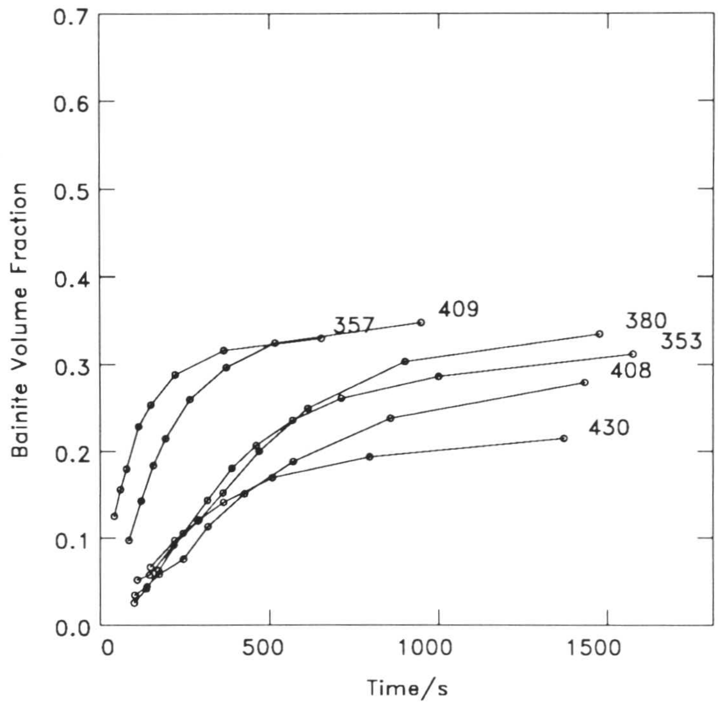

Figure 3.5 A plot of the isothermal transformation kinetics data obtained by Bhadeshia for the Fe–Mn–Si–C steel, as used for the optimisation of the original kinetics model (Bhadeshia, 1982b).

The experimental data were obtained by dilatometry, over a variety of temperatures within the bainitic transformation range. These length change data were analysed using the procedure outlined by Bhadeshia (1982b), given in Appendix 1. For each individual reaction the data were then normalised with respect to the maximum extent of reaction to produce datasets of normalised volume fraction ξ versus time t, for the purpose of evaluating the unknown constants.

Figures 3.5–3.7 show plots of the experimental isothermal transformation kinetics data obtained by Bhadeshia for the Fe–Mn–Si–C, Fe–Ni–Si–C and 300 M steels respectively. Of the three steels, 300 M shows the most consistent behaviour, with the other steels occasionally showing odd results for transformation under similar conditions. It is obvious that a mathematical model cannot reproduce results that are intrinsically inconsistent in this way.

In the case of the Fe–Mn–Si–C steel two transformation runs, at 409°C and 357°C gave particularly dubious results. The optimisation of the model was carried out after discarding those points, though the calculations were also carried out including the rogue points, in order to investigate their effect on the overall agreement.

3.3.7 Grain Size Measurement

The original model contains no account of the effect of the austenite grain size on trans-

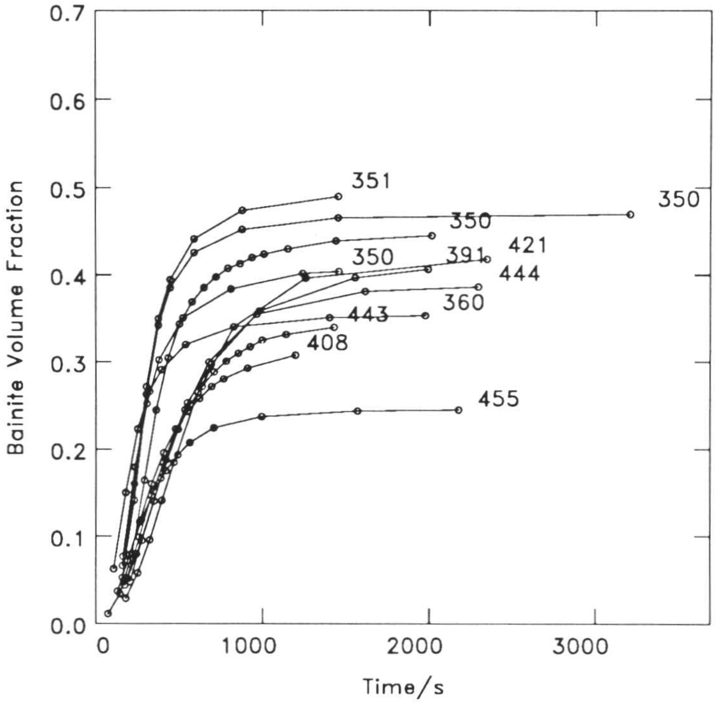

Figure 3.6 A plot of the isothermal transformation kinetics data obtained by Bhadeshia for the Fe–Ni–Si–C steel, as used for the optimisation of the original kinetics model (Bhadeshia, 1982b).

formation kinetics. In order to incorporate the effect, the austenite grain sizes produced in the three steels after austenitisation for 5 min at 1000°C were measured. The samples were quenched after austenitisation and then tempered for 1 hr at 600°C, in order to enhance the delineation of the prior austenite grains. The specimens were mounted, ground, polished and etched in 2% Nital for optical metallography. Grain size was represented by the mean linear intercept of a series of random lines with the grain boundaries, on scanning electron micrographs of the microstructure. Table 3.3 gives the results of the mean linear intercept measurements. The number of measurements was in each case 100, giving a statistical error of about ±10 %

Steel	Mean Linear Intercept/μm
Fe–Mn–Si–C	47 ±5
Fe–Ni–Si–C	52 ±6
300 M	86 ±9

Table 3.3 Mean Linear Intercept values for the austenite grain size of the high silicon steels, after austenitisation at 1000°C for 5 minutes.

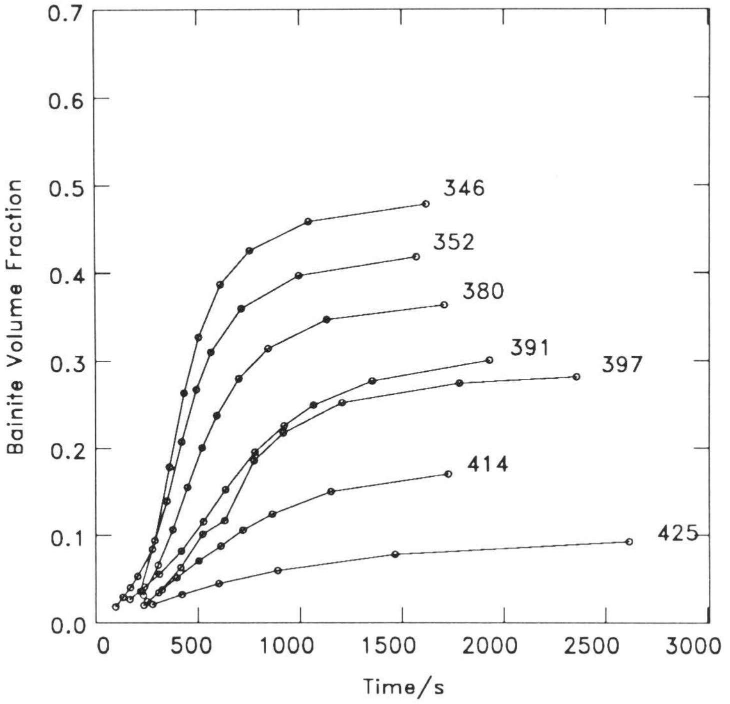

Figure 3.7 A plot of the isothermal transformation kinetics data obtained by Bhadeshia for the steel 300 M, as used for the optimisation of the original kinetics model (Bhadeshia, 1982b).

3.3.8 Numerical Analysis

To utilise the new model, it is necessary to determine four constants: K_1'/u, K_2, λ_1 and λ_2. This is one less than in the original model, because of the new condition which ensures that the nucleation rate is constant at W_S. Their values were adjusted to give the best agreement between the theory and the experimental data, subject to the condition that the sum

$$\sum \left(\ln\{t_p\} - \ln\{t_m\}\right) \tag{3.31}$$

is minimised, where t_p denotes the predicted reaction time and t_m denotes the experimental reaction time. The logarithm of these terms is taken because otherwise the error at larger time dominates the sum. A computer algorithm (given in Appendix 2) was developed to search downhill for a minimum to the above sum. The program was terminated when no significant improvements could be achieved.

In order to investigate the origin of any scatter in the agreement between predicted and experimental reaction times the model was optimised with respect to the data from each individual steel as well as with respect to the combined data from all the steels. In the case of the computer runs involving just one steel, there is no variation in the carbon content, and therefore the constant λ_2 was set to zero.

3.4 Results

Figure 3.8 shows plots of predicted versus experimental reaction times using the original and the new theory. The results for individual steels are shown in Figures 3.9–3.11. These plots correspond to steels Fe–Mn–Si–C, Fe–Ni–Si–C and 300 M respectively. The calculations are all summarised in Table 3.4.

Dataset	K_1'/u (m^2 s)	K_2(J mol^{-1})	λ_1	λ_2
Combined data	33.90×10^6	2.065×10^4	139.00	25.46
Fe–Mn–Si–C	38.76×10^6	1.925	4.756	0.00
Fe–Ni–Si–C	20.28×10^6	2.907×10^4	90.822	0.00
300 M	12.308×10^6	3.767×10^4	141.66	0.00

Table 3.4 Best fit values of constants after optimisation of the new theory using different datasets.

The effect of including the rogue data from the Fe–Mn–Si–C steel is shown in Figure 3.12a, which should be compared against Figure 3.8b. There is a deterioration in the overall agreement. Figure 3.12b (to be compared with Fig. 3.9) shows how the rogue data reduce the agreement with theory, for the Fe–Mn–Si–C on its own. Table 3.5 gives the best fit values for the constants when the rogue data are included in the numerical analysis.

Dataset	K_1'/u (m^2 s)	K_2(J mol^{-1})	λ_1	λ_2
Combined data	19.92×10^6	2.624×10^4	259.20	39.69
Fe–Mn–Si–C	19.18×10^6	6.395×10^3	9.696	0.00

Table 3.5 Best fit values of constants when the numerical analysis includes the rogue data in the Fe–Mn–Si–C experiments.

3.4.1 Application of The New Theory

The improvements due to the new analysis can be highlighted by comparison with the original model. Figure 3.13 shows the predicted transformation behaviour of Steels 1 and 2 at 470 °C. As can be seen, the high–manganese steel is now predicted as transforming slower than Steel 2, which has a smaller manganese concentration. Trends due to alloying element concentrations are therefore correctly predicted, unlike the data illustrated in Figure 3.2. Figure 3.14 shows the effect of temperature on the transformation behaviour of 300 M. The reaction kinetics are shown as increasing with decreasing temperature, as was observed experimentally, again

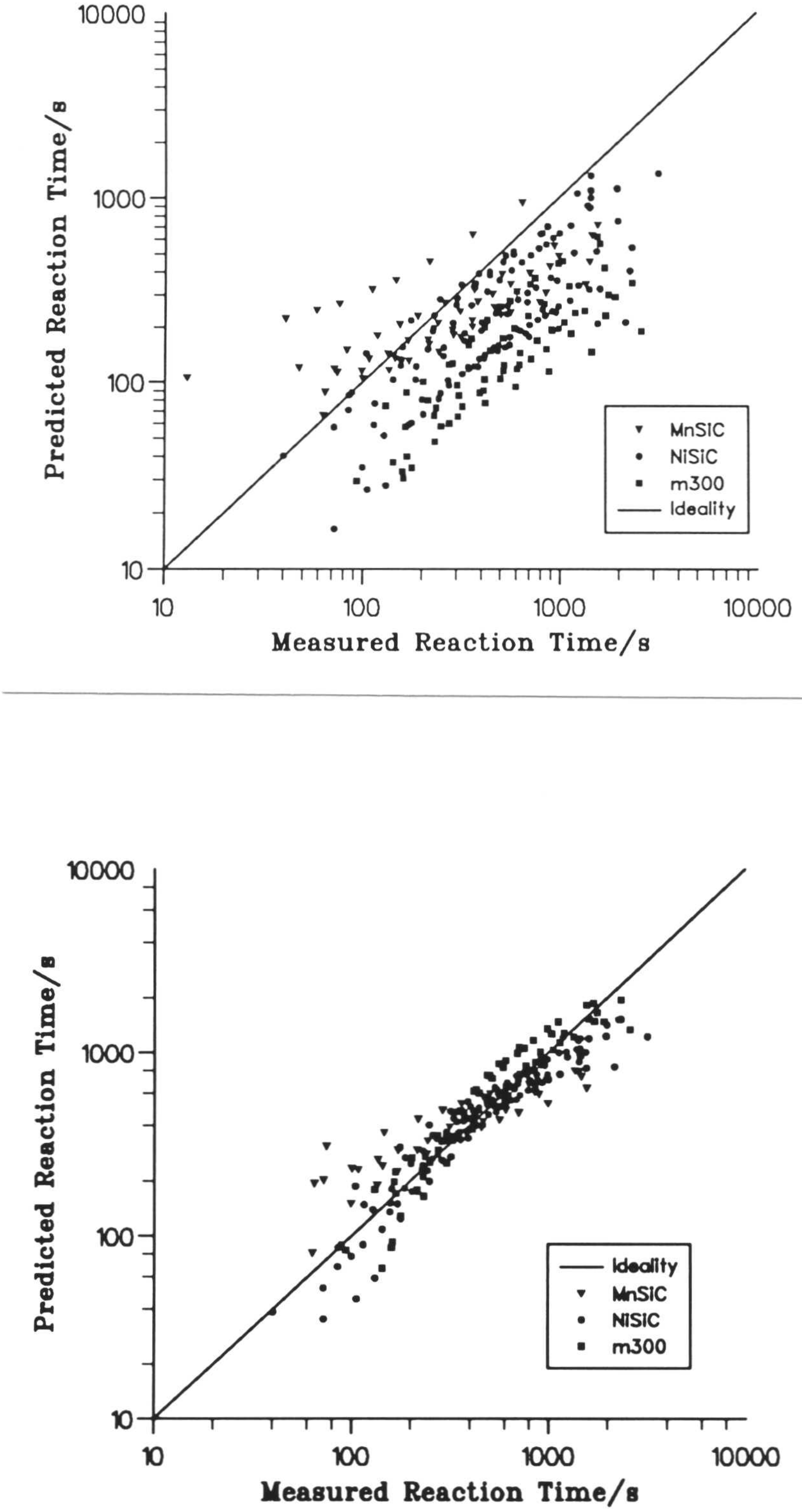

Figure 3.8 Comparison of predicted and experimentally determined reaction times for the bainite reaction in high silicon steels. a) Original theory. b) New theory.

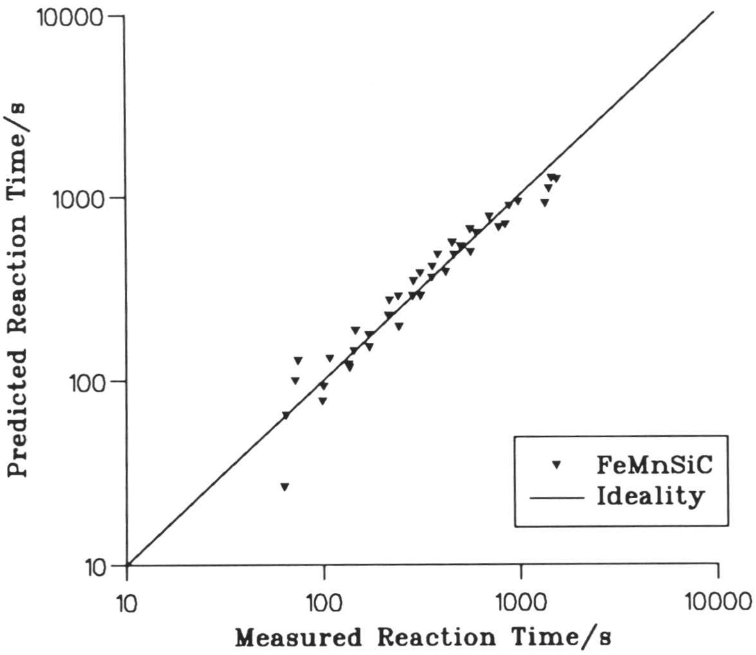

Figure 3.9 The degree of agreement between predicted and experimental reaction times for the steel Fe–Mn–Si–C after optimising the theory with respect to the data from this steel alone.

correcting the erroneous prediction by the original model. A computer program for calculating the isothermal reaction profiles of steels at temperatures below B_S is presented in Appendix 3. It can be seen by comparing the plots in Figure 3.8, that the new theory gives a significant improvement in the agreement between the measured and predicted reaction times. Data from each of the individual steels are also shown to be broadly consistent with the theory, though the constants derived by individual optimisation differ from those consistent with the best overall fit. The reasons for this effect are not clear and it is particularly worrying that the best fit constants for the Fe–Mn–Si–C steel are so different from the other alloys. Nevertheless, the form of the transformation curves is clearly well represented by the model.

The results can be summarised in a TTT diagram. Figure 3.15 shows the predicted TTT diagrams for Steel 1 and Steel 2, illustrating the fact that the manganese–rich steel transforms more slowly and that the reaction kinetics increase with decreasing temperature. A notable feature is that the predicted curves do not show the usual C-curve shape seen in some experimental diagrams. An examination of published TTT curve atlases reveals that this is not unexpected in high–hardenability alloys, although it is also worth pointing out that the present analysis takes no account of carbide precipitation, so that detailed comparisons are not in general possible.

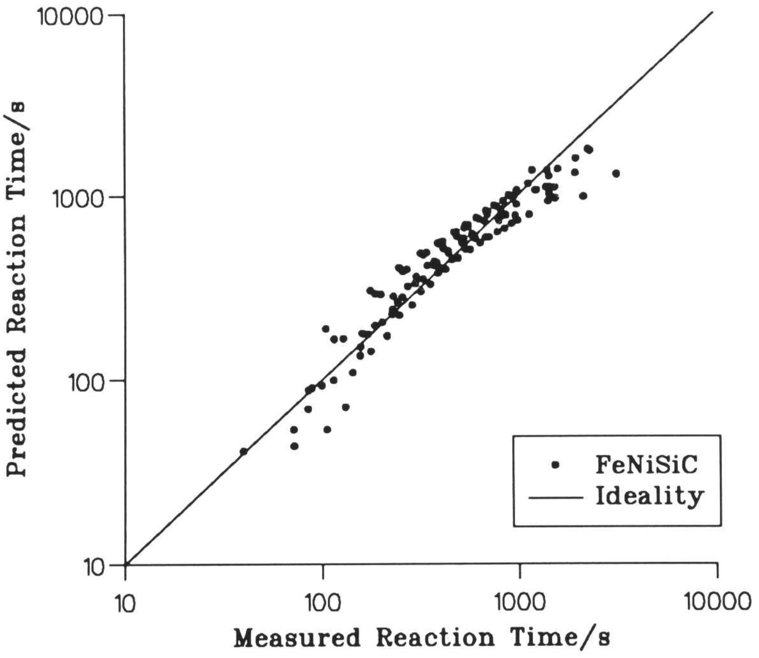

Figure 3.10 The degree of agreement between predicted and experimental reaction times for the steel Fe–Ni–Si–C after optimising the theory with respect to the data from this steel alone.

Most of the TTT curve data are on steels not used in the bainitic condition, whereas modern bainitic steels are designed to avoid carbide precipitation.

The absence of a C–shape could be real (as indicated by the experimental data for 300 M steel) or may be attributed to other factors which have been neglected. It has been consistently reported that the apparent thickness of bainitic sub–units varies as a function of the transformation temperature (Bhadeshia, 1982b; Pickering, 1958; Ohmori, Ohtani & Kunitake, 1971). It is not possible, however, to model this size variation without relaxing the condition that the steels have the same nucleation rate at W_S, though we have verified that such size variation would indeed result in a C-shaped TTT curve.

3.5 Conclusions

An earlier model for the overall transformation kinetics of bainite in steels where carbide precipitation can be suppressed, has been corrected and refined to be consistent with the known mechanisms of bainite nucleation and growth. The precision of the new model in estimating the rate of reaction is found to be better, and the model has a greater degree of internal consistency and one less disposable constant. The overall agreement between theory and experiment can be made good by optimising the values of four parameters, two of which describe autocatalysis, and

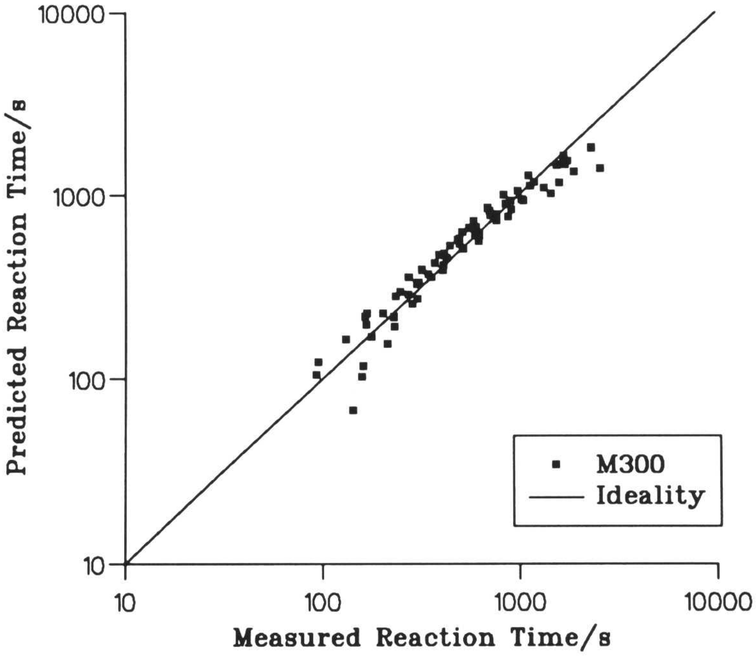

Figure 3.11 The degree of agreement between predicted and experimental reaction times for the steel 300 M after optimising the theory with respect to the data from this steel alone.

the other two describing the nucleation phenomena. It is suggested that these parameters can be used for all steels (where carbide formation is suppressed). Although much better agreement can be obtained when the parameter values are fixed by comparing the experimental data for just one steel against theory, the procedure is not justified because the parameters appear to vary haphazardly with alloy chemistry.

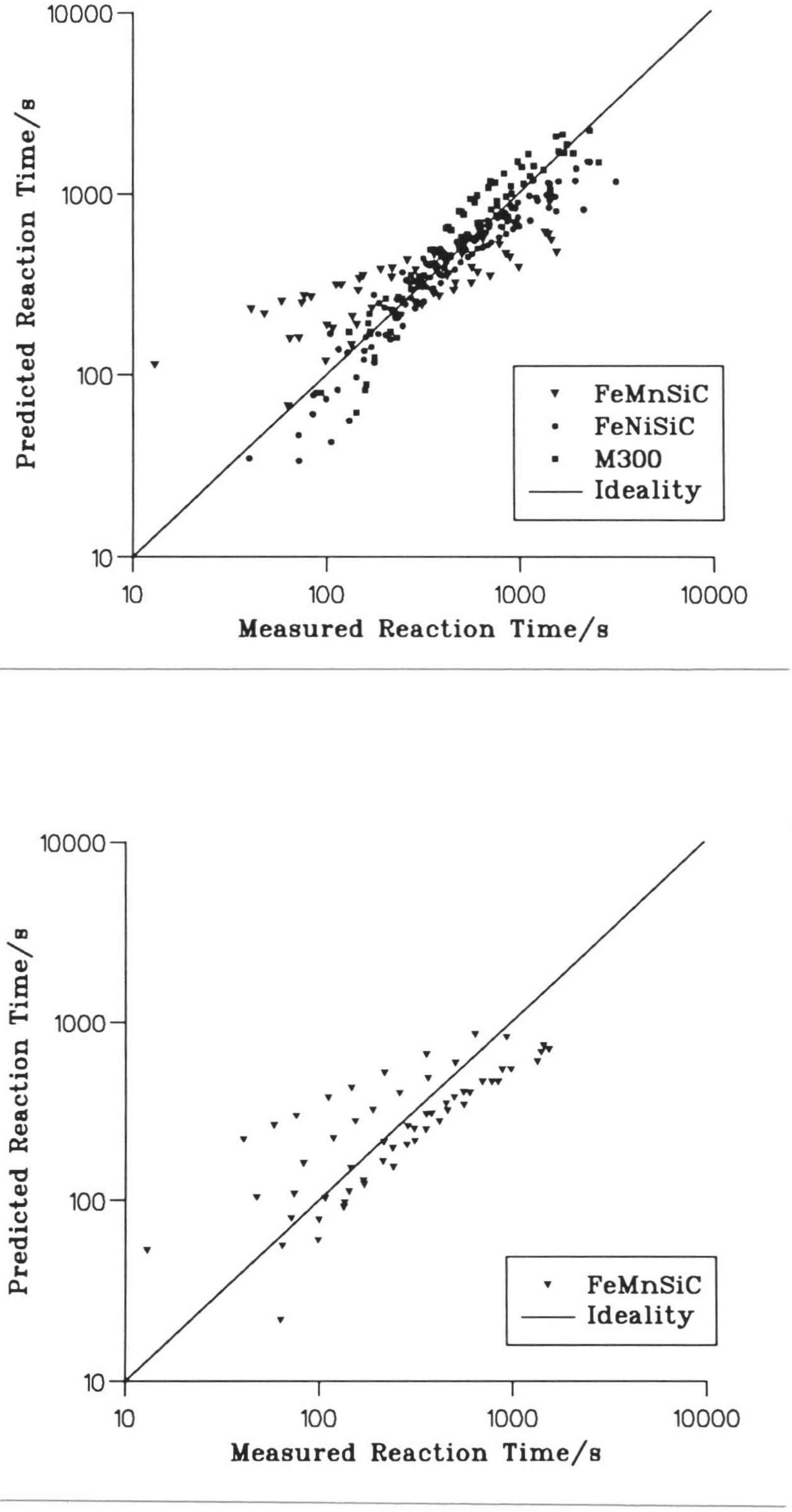

Figure 3.12 The effect on the degree of agreement with the new model of including the rogue data from Fe–Mn–Si–C. Plot (a) shows the deterioration in overall agreement. Plot (b) shows the best fit for the Fe–Mn–Si–C steels considered alone.

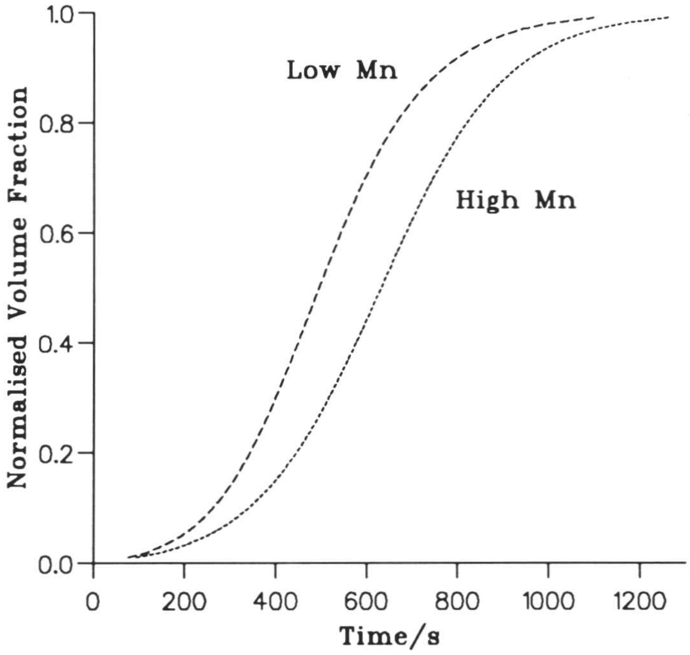

Figure 3.13 Comparison of the predicted reaction rates of Steel 1 and Steel 2, (compositions are given in Table 3.1) at 470°C using the new bainite kinetics model. The higher manganese content of Steel 2 results in a slower transformation, as expected, correcting the error in the original model.

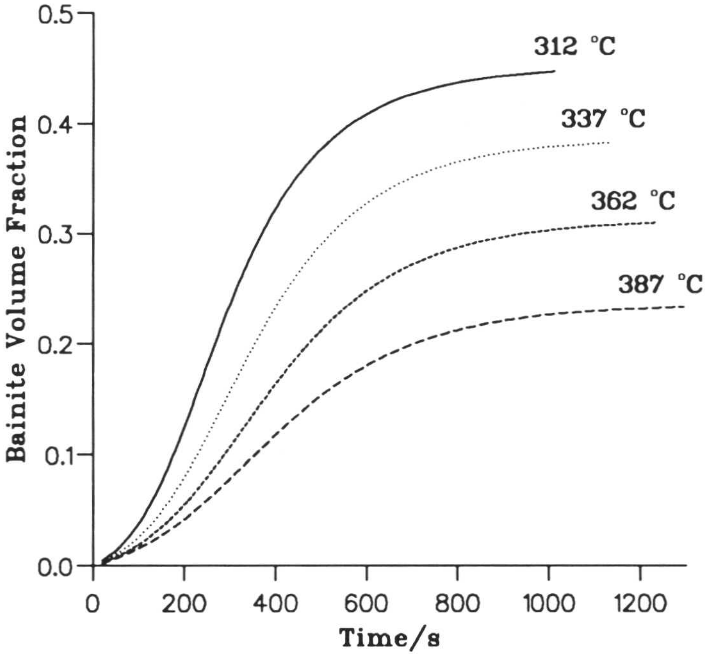

Figure 3.14 The predicted effect of temperature on the transformation of 300 M. The kinetics are predicted as increasing as temperature decreases, as observed experimentally, correcting the error in the original model.

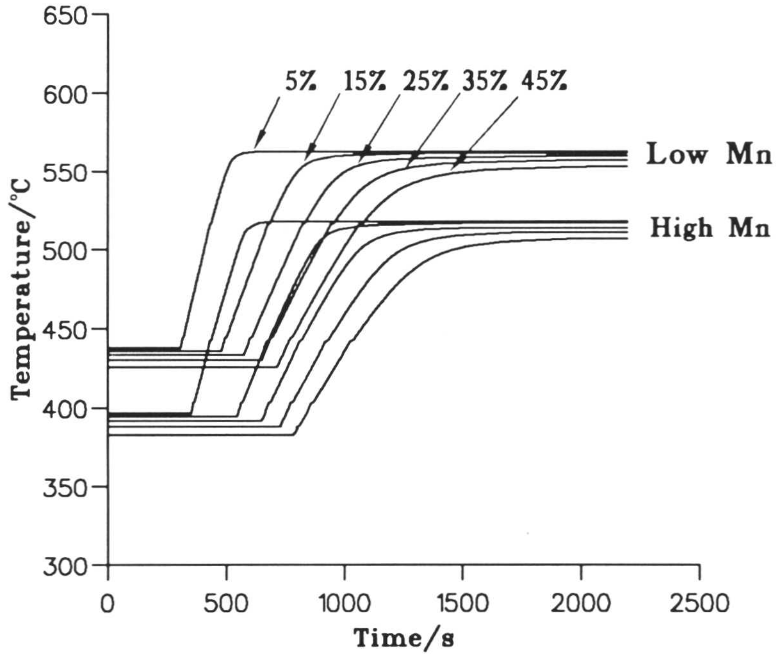

Figure 3.15 Comparison of the predicted TTT curves for Steel 1 and Steel 2 using the new model. The curves illustrate the prediction that highly alloyed steels react more slowly than lightly alloyed steels and that the reaction rate increases with undercooling below B_S.